NPL
National Physical Laboratory

Report

NPL REPORT
DQL-AC 011

The application of boundary element methods to near-field acoustic measurements on cylindrical surfaces at NPL

LOUISE WRIGHT, STEPHEN ROBINSON, VICTOR HUMPHREY, PETER HARRIS and GARY HAYMAN

NOT RESTRICTED

JANUARY 2005

dti
FUNDED BY THE DTI

National Physical Laboratory | Hampton Road | Teddington | Middlesex | United Kingdom | TW11 0LW

Switchboard 020 8977 3222 | **NPL Helpline** 020 8943 6880 | **Fax** 020 8943 6458 | **www.npl.co.uk**

The application of boundary element methods at NPL to near-field acoustic measurements on cylindrical surfaces

by

Louise Wright*, Stephen P. Robinson†,
Victor F. Humphrey‡, Peter M. Harris*, and Gary Hayman†

ABSTRACT

In this report, a description is given of work at the National Physical Laboratory to implement near-field techniques to characterise the far-field response of acoustic sources. The approach uses boundary-element methods to solve the integral form of the Helmholtz equation in order to predict the far-field response from discrete samples of the complex acoustic pressure measured on cylindrical surfaces. This has been done using a two-stage process, first deriving the required pressure gradient on the surface, and then calculating the desired far-field acoustic response. Both the Burton-Miller method and the CHIEF method have been implemented to overcome the uniqueness problem inherent in this method and a limited comparison made between them. To reduce computational size of the problem, use has been made of Fourier decomposition of the data from the scans. To speed up the computation, the NPL distributed computing network has been used to process the results for each of the Fourier coefficients, reducing the computational times by a factor of up to 20.

To undertake the near-field measurements, the NPL Open Tank facility was used. This is a state-of-the-art underwater acoustic test facility for undertaking high quality near-field scans. The facility benefits from a precision positioning system that operates under computer control to perform automated scans over designated surfaces in the near-field of an acoustic source. Measurements were made using a small probe hydrophone, with the amplitude and phase of the acoustic pressure recorded at discrete points on the cylindrical surface.

To exercise the method, measurements have been made of the field produced by a specially constructed directional source at frequencies of 13.9 kHz and 27.5 kHz. The results of the far-field predictions calculated from the near-field data have been validated by comparison with actual measurements made in the far-field, with agreement achieved of better than 1 dB over much of the acoustic beam-width. A discussion is presented of the influences on the accuracy of the method, and the possible causes of any discrepancies between predicted and measured results.

* Mathematics and Scientific Computing Group, Enabling Metrology Division, NPL
† Acoustics Team, Quality of Life Division, NPL
‡ Institute of Sound and Vibration Research, University of Southampton

ISSN 1744-0599

National Physical Laboratory
Teddington, Middlesex TW11 0LW

Approved on behalf of Managing Director, NPL, by Dr B. Zeqiri,
authorised by Director, Quality of Life Division.

CONTENTS

1. INTRODUCTION

The generation and detection of acoustic fields in water are typically undertaken using electroacoustic transducers, either deployed individually or in arrays. Such devices are most often characterised in terms of absolute sensitivity levels (important since source level and receive sensitivity are often used to determine range or detection limits) and device directivity (important for beam forming and for ambient noise rejection) [1,2].

Measurement of the transmit and receive sensitivity of transducers and arrays may be carried out in a variety of types of facility, for example laboratory tanks or open-water sites. At NPL, such facilities include laboratory tanks, the largest of which is a circular wooden tank of 5.5 m diameter and 5 m deep; an open-water facility located in 20 m deep water on a reservoir; and an Acoustic Pressure Vessel which can simulate ocean conditions for depths of up to 700 m and water temperatures from 2 ºC to 35 ºC.

The sensitivities and directional response are usually required to be determined in the acoustic far-field. However, if the array or transducer is physically large when measured in acoustic wavelengths (high ka value, where k is the wavenumber and a is the largest physical dimension), it may be impossible for far-field conditions to be achieved in a facility of finite size whilst maintaining free field environment and preserving steady state conditions [1,3]. An open-water facility will in general enable a greater source-receiver separation to be used, but such facilities have the disadvantage that there is little or no control of environmental conditions and, in any case, even an open-water facility will place some limit on the maximum separation achievable. Making measurements at sea is an extremely expensive alternative (often an order of magnitude more expensive than any tank or open-water measurements), provides no environmental control at all, and is usually reserved for evaluation of full system performance. There is consequently a strong motivation to maximise the range of acoustic testing possible in laboratory tanks.

One option to overcome the restrictions posed by finite-sized laboratory tanks is to undertake measurements in the acoustic near-field and then predict the acoustic far-field response from the near-field data. A number of techniques have been used for this purpose, and these are reviewed briefly in Section 2 of this report. The remainder of the report describes the work undertaken at NPL to use boundary-element methods to solve the integral form of the Helmholtz equation in order to predict the far-field response from discrete samples of the complex near-field acoustic pressure measured on cylindrical surfaces. This has been done using a two-stage process, first deriving the required pressure gradient on the surface, and then calculating the desired far-field acoustic response.

To make the near-field measurements, the NPL Open Tank facility was used. This is a state-of-the-art underwater acoustic measurement facility for undertaking near-field scans which benefits from a precision positioning system which operates under automated computer control. The facility also has excellent temperature stability.

To exercise the method, measurements have been made of the field produced by a specially constructed source at frequencies of 13.9 kHz and 27.5 kHz. Measurements of the magnitude and phase of the acoustic field were made using a small probe hydrophone which was scanned through the field, with the amplitude and phase of the acoustic pressure recorded at discrete points on the cylindrical surface. To reduce computational size of the problem, use has been made of Fourier decomposition of the data from the scans. To speed up the computation, the NPL distributed computing network has been used to process the results for each of the Fourier coefficients, reducing computational times by a factor of up to 20.

The report is structured as follows. After the review and description of methodology in Section 2, Section 3 states the mathematical formulation of the problem, in terms of both the Helmholtz equation and the boundary element method. Section 4 describes the software implementation and validation. Section 5 describes the experimental facility (the NPL open-tank facilities), the design of a test array used to exercise the method, and the measured data obtained using the facility. Section 6 shows the results obtained, and compares the predictions obtained with data measured in the acoustic far-field and on other surfaces in the near-field. Finally, Section 7 provides a summary of the conclusions from the work and points to improvements that might be made in the future.

2. METHODOLOGY

2.1 REVIEW OF NEAR-FIELD METHODS

There are a number of general techniques that have been applied to measurements in the acoustic near-field. For completeness, these are reviewed briefly here.

2.1.1 Use of boundary elements methods with the Helmholtz integral equation

In this method, the acoustic field is measured over a surface surrounding the source. Measurements may be made of any parameter which satisfies the wave equation, but most often the complex acoustic pressure is measured using a hydrophone. The surface is considered to be discretised, with the measured acoustic pressures representing the field over each of the discrete surface patches. The Helmholtz integral equation is then applied, the integral being solved numerically using boundary element methods to calculate the field exterior to the surface. Although in theory the surface may be of arbitrary shape, the measurements of the acoustic pressure are typically made over a simple surface such as a cylinder or sphere.

The theory may be formulated by considering that the propagation of acoustic waves of constant frequency in homogeneous media may be described using the Helmholtz wave equation:

$$\nabla^2 p + k^2 p = 0 \tag{2.1}$$

where the time dependence is suppressed and p is the acoustic pressure and k the wavenumber [4]. By use of Green's Second Theorem, this may be formulated as an integral equation over a closed surface:

$$p(\mathbf{r}) = \frac{1}{4\pi}\int_s \left[p(\mathbf{r}_o)\frac{\partial G\ (\mathbf{r},\mathbf{r}_o)}{\partial n} - G\ (\mathbf{r},\mathbf{r}_o)\frac{\partial p(\mathbf{r}_o)}{\partial n} \right] dS \tag{2.2}$$

where the acoustic pressure varies with location in the field, the location denoted by positional vector **r**, and where $\mathbf{r_0}$ is the location of a point on the surface and **r** is the location of a point *exterior* to the surface, n is a unit vector normal to the surface S, and the expression $G(\mathbf{r},\mathbf{r_0})$ is a Green's function which is a solution of the Helmholtz equation. The classic formulation given in Equation (2.2), termed the Helmholtz Integral Equation, is the starting point for much of the work applied to near-field measurements [5].

The above equation means that if the acoustic pressure distribution over a closed surface is known, for example from measurements made in the acoustic near-field over an appropriate surface, the pressure value anywhere else in the surrounding medium can be calculated. Most commonly, the Green's function is chosen to be the free-space fundamental solution to the Helmholtz equation:

$$G(\mathbf{r}/\mathbf{r}_o) = \frac{e^{+jkR}}{R} \tag{2.3}$$

where $r = |\mathbf{r} - \mathbf{r_0}|$ [5]. The Helmholtz Integral Equation requires that the acoustic pressure gradient be known in addition to the pressure. However, the pressure gradient is difficult to measure accurately in practice. Small pressure gradient sensors are difficult to construct, require a pair of well-matched transducers, and their finite size would tend to introduce significant spatial averaging of the field for higher frequencies. Consequently, a number of methods have been used to circumvent the need to measure the pressure gradient.

(i) Plane-wave approximation

One approach is to use the plane-wave approximation to the pressure gradient and this can provide a good approximation for surface geometries without high curvature and where the acoustic field does not vary rapidly over the surface [6,7]. However, the assumption is not generally valid and can lead to serious errors in the computed far-field response [6].

(ii) Use of alternative Greens' function

The need to measure the pressure gradient may be avoided if a different fundamental Green's function is used as a solution [3,8,9]. If appropriately chosen, the Green's function cancels itself out (and hence vanishes to zero) on the measurement surface, and the expression for the pressure p($\mathbf{r}$) then becomes:

$$p(\mathbf{r}) = \frac{1}{4\pi}\int_s p(\mathbf{r}_o)\frac{\partial G_k(\mathbf{r},\mathbf{r}_0)}{\partial n}dS \qquad (2.4)$$

In this case, the Green's function described by Equation (2.4) must satisfy the following condition for all points $\mathbf{r}$ on the surface S [3]:

$$G_k(\mathbf{r},\mathbf{r}_o) = g(\mathbf{r},\mathbf{r}_o) + \mathrm{X}(\mathbf{r}) = 0 \qquad (2.5)$$

The function g($\mathbf{r}$,$\mathbf{r}_o$) is defined over an infinite space, and the term X($\mathbf{r}$) must be adjusted so that Equation (2.5) is satisfied over a given geometry. Such functions can only have simple analytical solutions for plane, cylindrical or spherical measurement surfaces. However, although the use of this Green's function does not require knowledge of the pressure gradient and analytically eliminates the uniqueness suffered by some other methods rather elegantly, the function itself is highly complicated involving infinite series of spherical wave functions which cannot be solved analytically and which can be difficult to solve numerically. Thus, the elegance is offset by increased computational difficulties and the difficulties of knowing when to truncate the infinite series [10].

(iii) Deriving the pressure gradient numerically in a two-stage process

Another approach is to divide the process into two stages. Firstly, the integral equation is solved numerically to obtain the pressure gradient at each of the discrete measurement points. This can be achieved since the pressure is known, the Green's function is the free-space solution stated above and the gradient of the Green's function may be calculated. In the second stage, with the values of the pressure gradient now known, the integral equation is now solved numerically for the pressure at points in the far-field exterior to the surface. The numerical solution is computed by use of boundary element methods applied to the discretised surface. This is the method adopted at NPL.

An analytical problem arises in the solution to Equation (2.2) when the wavenumber (which appears in the Green's function) approaches an eigenfrequency of the associated internal problem, leading to non-uniqueness in the solution. This means that the solution is non-unique at the frequencies corresponding to the characteristic modes of the surface. Since the problem occurs only at the specific wavenumbers that correspond to the internal eigenfrequencies, it might be suggested that the problem be avoided by simply considering only wavenumbers which are not close to the eigenfrequancies. However, this is not a feasible solution for several reasons. Firstly, for an arbitrary surface shape the eigenfrequencies are not generally known *a priori* and so the internal problem would have to be solved in order to determine which wavenumbers to avoid. Secondly, the integral equation is discretised for numerical integration, which results in a system of algebraic equations so that there is no longer a specific value but a range of values at which the coefficient matrix becomes ill-conditioned, resulting in large numerical errors. Finally, the interval between successive eigenfrequencies decreases with increasing wavenumber (the "modal density" increases with frequency) such that it becomes impossible to stay sufficiently far away from the internal eigenvalues at high *ka* values [10].

Two approaches have been proposed to circumvent this difficulty: (a) those of Schenck [11] and Copley [12]; (b) those of Burton-Miller [13,14]. The first method overcomes the uniqueness problem by introducing additional equations derived from applying the Helmholtz formula applied at interior points, whereas the Burton-Miller approach does so by considering a linear combination of the surface Helmholtz integral equation and its differentiated form. This method has been variously known as the Helmholtz Gradient Formulation (HGF) or the Composite Outward Normal Derivative Overlap Relation (CONDOR), but is perhaps most often referred to simply as the Burton-Miller method [10,13-15].

2.1.2 Fourier-based methods

These methods decompose the acoustic field into a series of plane-waves, each travelling in a different direction, by use of two-dimensional spatial Fourier transforms [16]. The plane-waves are then propagated to a different separation distance and inverse Fourier transforms are used to regenerate the acoustic field at the new separation. The un-propagated Fourier transform is sometimes referred to as the plane-wave angular-spectrum and essentially represents the acoustic far-field in wavenumber space [16].

The measurements are typically performed by scanning a hydrophone over a planar surface with measurements made of the complex acoustic pressure at discrete points. This form of the method is most suitable for high-frequency directional fields [17-19]. Although this planar geometry is the most common implementation, the method may be extended to cylindrical or spherical surfaces with the mathematics then expressed in cylindrical or spherical coordinates [16,20].

One advantage of Fourier methods is the ease of which the field may be back-propagated toward the source. If the field is propagated back to the radiating surface, the source distribution may be obtained, though for a full description of the field at the radiating surface evanescent waves must be taken into account. This back-propagation technique can be useful to identify defects in transducers and malfunctioning elements in arrays. If the measurement surface is within only a few wavelengths of the radiating surface, the evanescent waves will also contribute to the measured field and the back-propagated reconstruction then has the potential for very high resolution. This technique is sometimes referred to as Near-field Acoustic Holography (NAH) [16].

NPL has successfully used the methods described above to characterise high frequency transducers and arrays at frequencies from 100 kHz to 500 kHz [21], and has compared the results with optical scans of the vibrating surface of a transducer obtained using a scanning laser vibrometer [22]. However, this work is described elsewhere and further discussion of it is beyond the scope of this report.

2.1.3 Near-field calibration array

The Near-Field Calibration Array (NFCA) method uses an array of hydrophones, the responses of which are weighted so as to produce a uniform plane wave in a given volume close to the array. The NFCA may consist of an array of planar transducers, but is often formed from an array of reciprocal hydrophones. The array may be used either in transmitting mode to generate a pseudo-plane-wave, or to spatially filter in receiving mode [23]. This type of array is sometimes referred to as a Trott array after W.J.Trott, one of the pioneers of this concept [24].

The NFCA method can employ a large hydrophone array containing numerous hydrophones arranged in line arrays or in concentric circles. The weighting is usually applied to the amplitude response only and is often provided by use of capacitors placed in parallel with each hydrophone. The weights are carefully calculated to produce the uniform plane wave field over a specific frequency range within a specified volume in front of the array, with the transducers to be calibrated placed within this volume. Rotating the transducer to be measured within this volume (or tilting the array itself) enables directivity measurements to be carried out. When the NFCA is used in receive mode, a transmitting device that is located in this volume will have only its far field planar component picked up by the NFCA, which then acts as a selective filter in the wavenumber domain [25].

The NFCA method is a powerful one which can produce accurate results quickly and without the need for sophisticated scanning systems. The technique has been used for frequencies up to 50 kHz, although it is more commonly used for frequencies less than 20 kHz. Disadvantages of the NFCA are the cost, since a large number of hydrophones (and acquisition channels) may be needed, the close matching of array elements that is required, and the potential for problems with inter-element interaction. These problems may be reduced by synthesising a planar array from a line array which is placed at successive locations in the field of the transducer under test [25]. The NFCA concept can also be extended to cylindrical and spherical geometries [26-28]. This is done using a line array for the cylindrical geometry, and a semi-circular array for the spherical geometry. In such cases, it is the transducer under test that is usually rotated to synthesise the array rather than scanning the NFCA array itself.

The NFCA method has not been attempted at NPL and is not discussed further in this report.

2.2 NPL IMPLEMENTATION USING THE HELMHOLTZ INTEGRAL

NPL has successfully used the Helmholtz integral method using method (iii) in Section 2.1.1 to solve the equation in a two-stage process, first deriving the required pressure gradient on the surface, and then evaluating the pressure in the acoustic far-field. Both the Burton-Miller method and the CHIEF method have been implemented to overcome the uniqueness problem and a comparison made between them.

To exercise the method, measurements have been made of the field produced by a specially constructed source array at frequencies of 13.9 kHz and 27.5 kHz. Measurements of the magnitude and phase of the acoustic field were made using a small probe hydrophone which was scanned through the field, with the amplitude and phase of the acoustic pressure recorded at discrete points. Cylindrical surfaces were used since the required degrees of freedom in order to undertake spherical surface scans were not available from the test tank positioning system. Often, it is more convenient if the source itself is rotated while the hydrophone remains fixed, and this the approach adopted at NPL. Essentially, the cylindrical surface is built up from a series of circular scans, with the depth of the hydrophone and/or source incremented after each circular scan. When undertaking the measurements, care must be taken to sample with sufficiently high spatial resolution to avoid aliasing problems, with the required sampling interval typically better than half an acoustic wavelength [29].

To reduce computational size of the problem, use has been made of Fourier decomposition of the data from each of the circular scans. To speed up the computation, use has been made of the NPL distributed computing network which has reduced the computational times by a factor of up to 20.

A description of this work forms the bulk of this report.

3. MATHEMATICAL FORMULATION OF THE PROBLEM

This Section presents the background to using the *Boundary Element Method (BEM)* for predicting the far-field characteristics of the sound field radiated by a hydrophone submerged in water given measurements made in the acoustic near-field. The method used is that described Section 2.1.1 (iii).

There are two stages in the application of the boundary element method to this problem. The first step is to formulate the problem as a surface integral equation, where we require that the integral equation involves integral operators that are non-singular and well-conditioned for all wavenumbers encountered. The mathematical formulation of the problem is considered in Section 3.1. The second step is to apply a numerical technique to solve the surface integral equation, based on approximating the boundary surface and the solution field defined over this surface. This is the subject of Section 3.2.

3.1 THE HELMHOLTZ INTEGRAL EQUATION

The propagation of small amplitude acoustic waves in a fluid surrounding a radiating or scattering surface, as shown in Figure 3.1, is governed by the linear wave equation

$$\nabla^2\Psi = \frac{1}{c^2}\frac{\partial^2\Psi}{\partial t^2} \tag{3.1}$$

where $\Psi(\mathbf{p},t)$ is a scalar velocity potential depending on position $\mathbf{p}$ and time t, and c is the wave propagation velocity.

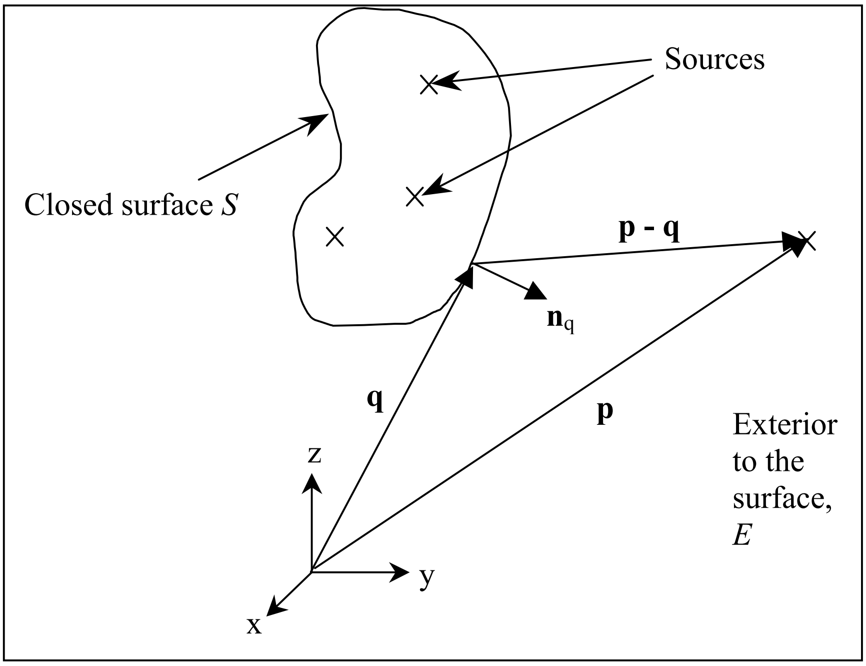

Figure 3.1 Geometry of the problem

The sound pressure of a fluid of density ρ is then given in terms of the velocity potential by

$$P = -\rho \frac{\partial \Psi}{\partial t}.$$

If we assume single frequency time harmonic dependence of the form

$$\Psi(\mathbf{p}, t) = \varphi(\mathbf{p}) e^{-i\omega t},$$

where $\omega = kc$, $k = 2\pi/\lambda$ is the wavenumber, and λ is the wavelength, then φ, which is a complex-valued function of position $\mathbf{p}$ only, satisfies the Helmholtz equation

$$\nabla^2 \varphi + k^2 \varphi = 0. \tag{3.2}$$

This equation is identical to Equation (2.1). The parameter φ could be regarded as the velocity potential or the pressure, since the two are related by a simple scale factor. In addition, φ is required to satisfy a boundary condition on some closed piecewise smooth surface *S*. This condition could be a Dirichlet condition

$$\varphi(\mathbf{p}) = f(\mathbf{p}), \quad \mathbf{p} \in S, \tag{3.3}$$

a Neumann condition

$$\frac{\partial}{\partial n} \varphi(\mathbf{p}) = f(\mathbf{p}), \quad \mathbf{p} \in S, \tag{3.4}$$

where n is the outward normal to S at $\mathbf{p}$, or a general Robin boundary condition

$$\alpha(\mathbf{p})\varphi(\mathbf{p}) + \beta(\mathbf{p}) \frac{\partial}{\partial n} \varphi(\mathbf{p}) = f(\mathbf{p}), \quad \mathbf{p} \in S, \tag{3.5}$$

where α, β and f are given (complex-valued) functions defined on the surface *S*.

The closed surface *S* divides space into two regions: *D*, the interior to the surface, and *E*, the exterior to the surface. If the problem to be solved requires values in *E* to be calculated (an *exterior* problem), then the problem requires a condition that the scattered and radiated waves are out-going: this is the Sommerfeld radiation condition, viz.,

$$\lim_{r \to \infty} r^{1/2} \left(\frac{\partial \varphi}{\partial r} - ik\varphi \right) = 0 \tag{3.6}$$

in two dimensions, and

$$\lim_{r \to \infty} r \left(\frac{\partial \varphi}{\partial r} - ik\varphi \right) = 0 \tag{3.7}$$

in three dimensions, where r is the length of the position vector $\mathbf{p}$ relative to some origin.

3.1.1 Green's functions and potential operators

The solution of Equation (3.2) using the boundary element method will require use of the appropriate Green's function. The Green's function for the Helmholtz equation is the function $G_k(\mathbf{p}, \mathbf{q})$ that satisfies in both variables the equation

$$\nabla^2 G_k(\mathbf{p},\mathbf{q}) + k^2 G_k(\mathbf{p},\mathbf{q}) = -\delta(\|\mathbf{p}-\mathbf{q}\|),$$

where δ is the Dirac delta function, and the Sommerfeld radiation condition. The Green's function is defined by

$$G_k(\mathbf{p},\mathbf{q}) = \frac{i}{4} H_0^{(1)}(kr)$$

in two dimensions, and

$$G_k(\mathbf{p},\mathbf{q}) = \frac{1}{4\pi}\frac{e^{ikr}}{r}$$

in three dimensions, where $r = \|\mathbf{p} - \mathbf{q}\|$ and $H_0^{(1)}$ is the Hankel function of the first kind of order zero. $G_k(\mathbf{p}, \mathbf{q})$ represents the effect observed at a point $\mathbf{p}$ of a unit source at the point $\mathbf{q}$ (or vice versa).

As has been stated in Section 2, the problem of interest is the exterior problem for which $\mathbf{p}$ lies in E. If Equation (3.2) is multiplied by $G_k(\mathbf{p}, \mathbf{q})$ and the result is integrated for fixed $\mathbf{p}$ and varying $\mathbf{q}$ over the volume E, and the Sommerfeld radiation condition is applied, it can be shown that

$$\int_S \varphi(\mathbf{q})\frac{\partial}{\partial n_q}G_k(\mathbf{p},\mathbf{q}) - G_k(\mathbf{p},\mathbf{q})\frac{\partial}{\partial n_q}\varphi(\mathbf{q})dS_q = \begin{cases} \frac{1}{2}\varphi(\mathbf{p}), & \mathbf{p}\in S, \\ \varphi(\mathbf{p}), & \mathbf{p}\in E, \end{cases} \tag{3.8}$$

where

$$\frac{\partial}{\partial n_q}\varphi(\mathbf{q}) = \nabla\varphi.\mathbf{n}_q$$

and $\mathbf{n}_q$ is the normal to the surface S. This is a more generalised statement of Equation (2.2).

It is useful for the direct and indirect integral equation formulations given below for equation (3.8) to define single- and double-layer Helmholtz potential operators by, respectively,

$$\{L_k\sigma\}(\mathbf{p}) = \int_S \sigma(\mathbf{q})G_k(\mathbf{p},\mathbf{q})dS_q$$

and

$$\{M_k\sigma\}(\mathbf{p}) = \int_S \sigma(\mathbf{q}) \frac{\partial}{\partial n_q} G_k(\mathbf{p},\mathbf{q}) dS_q ,$$

where σ is a twice continuously differentiable function defined on each part of S.

We shall also need the normal derivatives of these potentials:

$$M_k^{\mathrm{T}}\sigma \equiv \frac{\partial}{\partial n_p} L_k \sigma = \int_S \sigma(\mathbf{q}) \frac{\partial}{\partial n_p} G_k(\mathbf{p},\mathbf{q}) dS_q$$

and

$$N_k\sigma \equiv \frac{\partial}{\partial n_p} M_k\sigma = \frac{\partial}{\partial n_p} \int_S \sigma(\mathbf{q}) \frac{\partial}{\partial n_q} G_k(\mathbf{p},\mathbf{q}) dS_q .$$

The potentials L_k and N_k are continuous as $\mathbf{p}$ crosses S, but M_k^{T} and M_k experience jump discontinuities of the following forms:

$$\begin{aligned} \lim_{\mathbf{q}\to\mathbf{p}} \frac{\partial}{\partial n_p} L_k\sigma(\mathbf{q}) &= -\frac{1}{2}\sigma(\mathbf{p}) + \frac{\partial}{\partial n_p} L_k\sigma(\mathbf{p}), \quad \mathbf{p} \in S, \quad \mathbf{q} \in E, \\ \lim_{\mathbf{q}\to\mathbf{p}} \frac{\partial}{\partial n_p} L_k\sigma(\mathbf{q}) &= +\frac{1}{2}\sigma(\mathbf{p}) + \frac{\partial}{\partial n_p} L_k\sigma(\mathbf{p}), \quad \mathbf{p} \in S, \quad \mathbf{q} \in D, \end{aligned} \tag{3.9}$$

and

$$\begin{aligned} \lim_{\mathbf{q}\to\mathbf{p}} M_k\sigma(\mathbf{q}) &= +\frac{1}{2}\sigma(\mathbf{p}) + M_k\sigma(\mathbf{p}), \quad \mathbf{p} \in S, \quad \mathbf{q} \in E, \\ \lim_{\mathbf{q}\to\mathbf{p}} M_k\sigma(\mathbf{q}) &= -\frac{1}{2}\sigma(\mathbf{p}) + M_k\sigma(\mathbf{p}), \quad \mathbf{p} \in S, \quad \mathbf{q} \in D. \end{aligned}$$

3.1.2 Direct Integral Equation Formulation

Suppose that $\mathbf{p}$ lies on the surface S. Then in operator notation, Equation (3.8) takes the form

$$\left(M_k - \frac{1}{2} I \right) \varphi = L_k \frac{\partial \varphi}{\partial n}, \quad \mathbf{p} \in S, \tag{3.10}$$

where I is the identity operator. This equation is known as the surface Helmholtz integral equation.

In the case of the Neumann boundary condition of Equation (3.4), the surface Helmholtz equation takes the form of a Fredholm integral equation of the second kind for φ, viz.,

$$\left(-\frac{1}{2}I+M_k\right)\varphi=L_k f,\quad \mathbf{p}\in S. \qquad (3.11)$$

Having solved the surface Helmholtz equation to determine φ on S, the values of φ at points in E are then computed from

$$\varphi=M_k\varphi-L_k\frac{\partial}{\partial n}\varphi,\quad \mathbf{p}\in E, \qquad (3.12)$$

which is the Helmholtz formula for $\mathbf{p}\in E$ expressed using operator notation.

Direct integral equation formulations may be similarly derived for the Dirichlet and general Robin boundary conditions.

3.1.3 Indirect Integral Equation Formulation

A solution to the problem is sought in the form of a single layer potential, viz.,

$$\phi(\mathbf{p})=L_k\sigma(\mathbf{p}),\quad \mathbf{p}\in E. \qquad (3.13)$$

Now, from (3.9),

$$\lim_{\mathbf{q}\to\mathbf{p}}\frac{\partial}{\partial n_p}L_k\sigma(\mathbf{q})=-\frac{1}{2}\sigma(\mathbf{p})+\frac{\partial}{\partial n_p}L_k\sigma(\mathbf{p})=-\frac{1}{2}\sigma(\mathbf{p})+M_k^{\mathrm{T}}\sigma(\mathbf{p}),\quad \mathbf{p}\in S,\quad \mathbf{q}\in E,$$

and so substituting in the Neumann boundary condition (3.4) we obtain

$$-\frac{1}{2}\sigma(\mathbf{p})+M_k^{\mathrm{T}}\sigma(\mathbf{p})=f(\mathbf{p}),\quad \mathbf{p}\in S,$$

that is,

$$\left(-\frac{1}{2}I+M_k^{\mathrm{T}}\right)\sigma(\mathbf{p})=f(\mathbf{p}),\quad \mathbf{p}\in S. \qquad (3.14)$$

This is an integral equation for the surface density σ. Having solved (3.14) to determine σ, the values of φ at points in E are then computed from (3.13).

A formulation is also possible involving a double layer representation, viz.,

$$\phi(\mathbf{p})=M_k\sigma(\mathbf{p}),\quad \mathbf{p}\in E.$$

These layer potential methods for obtaining an integral equation representation of the solution to the Helmholtz equation are *indirect* formulations since the resulting integral equation is not solved directly for a field quantity such as φ but for a layer density σ that has no physical significance.

Indirect integral equation formulations may be similarly derived for the Dirichlet and general Robin boundary conditions.

3.1.4 Uniqueness issues

It can be shown that under quite mild assumptions, the solution to the exterior Helmholtz equation (3.2) subject to one of the boundary conditions (3.3)–(3.5) and the Sommerfield radiation condition (3.6) or (3.7) is unique. Unfortunately, this property is *not* inherited by the integral equation formulations described above. When the wavenumber k takes critical values the operators are singular and the formulations in their present form no longer hold. The nature of the failure is different for the direct and indirect formulations. For the former, the integral Equation (3.11) always has a solution but it is non-unique for the critical wavenumbers, whereas for the latter, the integral Equation (3.14) for the surface density σ may have no solution at the same wavenumbers because the assumed representation as a single layer potential is invalid.

The critical wavenumbers are those discrete real values k for which the interior Helmholtz equation with a homogeneous Dirichlet boundary condition, viz.,

$$\nabla^2\varphi + k^2\varphi = 0, \quad \mathbf{p} \in D,$$

subject to

$$\varphi = 0, \quad \mathbf{p} \in S,$$

has non-trivial solutions. It is well-known that this problem has a non-trivial solution for a countably infinite set K of values k that correspond to the eigenfrequencies (the standing-waves or modal frequencies) of the interior volume D. These functions are used to construct non-trivial solutions to the homogeneous forms of the integral equation formulations of the exterior problem, and to infer the singularity of the corresponding integral operators for $k \in K$.

Given $k \in K$, let θ be a non-trivial solution to the above homogeneous interior problem. Then, it can be shown that for $\mathbf{p} \in S$,

$$\left(-\frac{1}{2}I + M_k^{\mathrm{T}}\right)\varphi = 0,$$

where

$$\varphi = \frac{\partial}{\partial n}\theta, \quad \mathbf{p} \in S,$$

and φ is not identically zero over S. This means that for $k \in K$ the integral operator

$$\left(-\frac{1}{2}I + M_k^{\mathrm{T}}\right)$$

is *singular*, and the integral Equation (3.14) will possess no solution or a non-unique solution depending on whether f in (3.14) lies inside or outside the null space of the integral operator. (The null space is the set of functions that are annihilated by the operator.)

On the other hand, given $k \notin K$, there are no non-trivial functions φ such that for **p** on S,

$$\left(-\frac{1}{2}I + M_k^{\mathrm{T}}\right)\varphi = 0.$$

This means that for $k \notin K$ the integral operator is *non-singular* and the integral equation (3.14) possesses a *unique* solution.

For wavenumbers close to the critical values K, the integral operator is ill-conditioned, and approximate solutions to the integral equations can be expected to be unreliable. The problem is made worse at higher frequencies for which the density of the critical values increases. Consequently, there is a requirement for alternative and improved formulations that provide unique solutions for all values of k and that are well-conditioned. We indicate below two popular improved formulations: the combined Helmholtz integral equation formulation (CHIEF) and the Burton-Miller formulation.

3.1.4.1 Combined Helmholtz Integral Equation Formulation (CHIEF)

In this formulation [11,12], the surface Helmholtz integral Equation (3.10) is supplemented by the Helmholtz formula applied at interior points, and the combined system

$$\left(M_k - \frac{1}{2}I\right)\varphi = L_k \frac{\partial \varphi}{\partial n}, \quad \mathbf{p} \in S,$$

and

$$M_k \varphi = L_k \frac{\partial \varphi}{\partial n}, \quad \mathbf{p} \in D, \tag{3.15}$$

is solved. It can be shown that there is always a unique solution if (3.15) holds at all points **p** lying in D. In practice, (3.15) can only be enforced at a finite number of points and if these points are chosen badly, then the additional equations fail to provide the necessary constraint to ensure uniqueness.

3.1.4.2 Formulation of Burton and Miller

Differentiation of the surface Helmholtz integral equation (3.10) gives

$$N_k \varphi = \left(\frac{1}{2}I + M_k^T\right)\frac{\partial \varphi}{\partial n}, \quad \mathbf{p} \in S. \tag{3.16}$$

The formulation originating with Alan Burton and Geoff Miller (hereafter called the Burton-Miller method formulation) [10, 13-15] comes from considering the following linear combination of the surface Helmholtz integral equation (3.10) with (3.16):

$$\left(-\frac{1}{2}I + M_k + \mu N_k\right)\varphi = \left[L_k + \mu\left(\frac{1}{2}I + M_k^T\right)\right]\frac{\partial \varphi}{\partial n}, \quad \mathbf{p} \in S, \tag{3.17}$$

where μ is a coupling constant. It can be shown that this integral formulation has a unique solution provided μ is strictly complex.

3.1.5 Axisymmetric structures with non-symmetric data

If the surface S is axisymmetric and the data that is measured on it is independent of θ, so that $\varphi = \varphi(r, z)$, then the problem can be treated as a two-dimensional one and the computational expense can be significantly reduced.

As was stated in Section 2, the near-field data are measured at a set of points lying on a cylinder, so that the pressure data are of the form $\{p(\theta_i, z_j), i = 1, 2, \ldots, n, j = 1, 2, \ldots, m\}$. Although the measurement data are not generally axisymmetric, each ring of constant z can be written as a sum of axisymmetric functions by using a Fourier series, so that

$$\begin{aligned} p(\theta_i, z_j) &= \hat{p}_j(\theta_i) \\ &= b_0^j + \sum_{k=1}^{\infty}\left(a_k^j \sin k\theta_i + b_k^j \cos k\theta_i\right), \qquad i = 1,2,\ldots,n,\ j = 1,2,\ldots,m. \end{aligned} \tag{3.18}$$

Each term in the Fourier series can be propagated separately, provided an altered form of the Green's function is used, as described by Macey [30]. The proof is given in full in Appendix 1. Care needs to be taken when using this formulation in conjunction with the Burton-Miller method since the derivative of the modified Green's function required for N_k can be difficult to calculate.

3.2 THE BOUNDARY ELEMENT METHOD

In general, the equations used in the CHIEF method ((3.10) and (3.15)), and in the Burton-Miller Method ((3.17)), cannot be solved analytically. Hence, it is necessary to use a numerical method to generate an approximate solution. The numerical method most commonly used for problems, such as this one, that involve surface integrals is the Boundary Element Method (BEM).

The basis of the boundary element method is to replace the integral Equation (3.10) or (3.17) by a linear algebraic system of equations: the integral operators are replaced by matrices, and the boundary functions by vectors. One technique for doing this replacement is *collocation*, and the technique in its simplest form, i.e., C^0-collocation, is described below [31].

3.2.1 Formulation of the BEM equations

To begin with, the boundary S is replaced by a set of non-overlapping panels S_j:

$$S \approx \bigcup_{j=1}^{n} S_j. \tag{3.25}$$

The panels will usually have a characteristic form. For example, in two-dimensions S_j often takes the form of a straight-line segment, and in three-dimensions a planar triangle. Usually, the replacement of S by the set of panels S_j is an *approximate* one, the quality of the approximation often depending on the choice of n.

The C^0-collocation method involves representing the boundary functions by a constant on each panel, i.e.,

$$\varphi(\mathbf{p}) = u_j, \quad \frac{\partial}{\partial n}\varphi(\mathbf{p}) = v_j, \quad \forall \mathbf{p} \in S_j. \tag{3.26}$$

The constant value is taken to be the value of the boundary function at some representative point, the collocation point, on the panel S_j. The combination of the representation of the panels S_j and the approximation of the boundary functions over the panels defines the *element* in the boundary element method. More complicated elements can have higher orders of approximation for the boundary function, such as linear variation across the panel. Now, using Equation (3.25) and Equation (3.26), the operator L_k, for example, is replaced by

$$L_k\varphi = \sum_j \int_{S_j} \varphi(\mathbf{q}) G_k(\mathbf{p},\mathbf{q}) dS_q = \sum_j u_j \int_{S_j} G_k(\mathbf{p},\mathbf{q}) dS_q = \sum_j u_j L_{k,j} e, \quad \mathbf{p} \in S,$$

where e is the unit function, and $L_{k,j}$ is the operator L_k applied over panel S_j. It follows that Equation (3.17) is replaced by its discrete form

$$\sum_j u_j \left(-\frac{1}{2} I + M_{k,j} + \mu N_{k,j} \right) e = \sum_j v_j \left[L_{k,j} + \mu \left(\frac{1}{2} I + M_{k,j}^{\mathrm{T}} \right) \right] e, \quad \mathbf{p} \in S. \tag{3.27}$$

Finally, evaluating Equation (3.27) at each collocation point $\mathbf{p}_j \in S_j$, $j = 1, \ldots, n$, we obtain a system of equations of the form

$$\left(-\frac{1}{2}\hat{I} + \hat{M} + \mu\hat{N} \right)\mathbf{u} = \left[\hat{L} + \mu \left(\frac{1}{2}\hat{I} + \hat{M}^{\mathrm{T}} \right) \right] \mathbf{v}, \tag{3.28}$$

where

$$\mathbf{u} = (u_1, \ldots, u_n)^{\mathrm{T}},$$
$$\mathbf{v} = (v_1, \ldots, v_n)^{\mathrm{T}},$$

and, for example, the (i, j)th element of the matrix $\hat{L}$ is

$$[\hat{L}]_{ij} = L_{k,j} e, \quad \mathbf{p} = \mathbf{p}_i.$$

The key to the implementation of the boundary element method for solving Equation (3.17), therefore, is the evaluation of the discrete integral operators

$$
\begin{aligned}
L_{k,j}e &= \int_{S_j} G_k(\mathbf{p},\mathbf{q})dS_q, && \text{(a)}\\
M_{k,j}e &= \int_{S_j} \frac{\partial}{\partial n_q} G_k(\mathbf{p},\mathbf{q})dS_q, && \text{(b)}\\
M^{\mathrm{T}}_{k,j}e &= \frac{\partial}{\partial n_p}\int_{S_j} G_k(\mathbf{p},\mathbf{q})dS_q, && \text{(c)}\\
N_{k,j}e &= \frac{\partial}{\partial n_p}\int_{S_j} \frac{\partial}{\partial n_q} G_k(\mathbf{p},\mathbf{q})dS_q, && \text{(d)}
\end{aligned}
\qquad (3.29)
$$

given $\mathbf{p}$ and n_p. The derivative operator in (3.29c) can always be carried inside the integral, and the same is true for (3.29d) provided $\mathbf{p} \notin S_j$. When $\mathbf{p} \notin S_j$, the discrete integral operators in (3.29) are all regular, and standard quadrature rules may be used for their evaluation. When $\mathbf{p} \in S_j$, the operators (3.29b) and (3.29c) are regular, but the operators (3.29a) and (3.29d) require special treatment. It is this aspect that makes implementation of the Burton-Miller formulation of the Helmholtz surface integral equation difficult. Approaches to evaluating the operators (3.29a) and (3.29d), based on isolating the singularity when $\mathbf{p} = \mathbf{q}$, are given in the literature [13, 31-33].

If the CHIEF method is used, only (3.29a) and (3.29b) are required, and the system of equations will be of the form

$$
\begin{bmatrix} -\frac{1}{2}\hat{I} + \hat{M} \\ \tilde{M} \end{bmatrix} \mathbf{u} = \begin{bmatrix} \hat{L} \\ \tilde{L} \end{bmatrix} \mathbf{v}, \qquad (3.30)
$$

where

$$
[\tilde{L}]_{ij} = L_{k,j}e, \quad \mathbf{p} = \mathbf{w}_i,
$$

and $\mathbf{w}_i$ are the internal points used to define the conditions in Equation (3.15). The system of Equations (3.30) is over-determined as there are more equations than there are variables. The operators are all regular for $\mathbf{p} \in D$, so the extra conditions of Equation (3.15) do not cause any additional difficulties.

3.2.2 Solving the BEM equations

Generally, to give a good approximation to the solution of the Helmholtz equation, the maximum dimension of any of the panels must be less then $^1/_2$ of the wavelength λ. If the surface to be modelled is large and the frequency of interest is high, this can lead to very large matrices appearing in Equation (3.28) and Equation (3.30).

For general surfaces S and choice of boundary elements S_j, the matrices $\hat{L}$, $\hat{M}$, $\hat{M}^{\mathrm{T}}$ and $\hat{N}$ are full and without structure. To solve the linear algebraic Equations (3.28) a full matrix method, such as based on an LU matrix decomposition [34], is used.

For high frequency problems, this method can be very computationally expensive, both in terms of CPU time and memory requirements. As was stated in the previous Section, the Equations (3.30) are over-determined and so can only be solved in a least-squares sense. More information on least-squares solvers is available in the literature, for example in Golub and van Loan [34], or Lawson and Hanson [35].

However, for a *rotationally symmetric* surface S and choice of boundary elements S_j, the matrices are full but exhibit a particular structure that may be exploited to improve the memory requirements for storing the matrices as well as the cost of solving Equation (3.28) and Equation (3.30).

Let the axisymmetric surface S be approximated by n_s strips T_α, each composed of n_e elements $S_{\alpha\beta}$, so that

$$n = n_s n_e, \quad T_\alpha = \bigcup_{\beta=1}^{n_e} S_{\alpha\beta}, \quad S = \bigcup_{\alpha=1}^{n_s} T_\alpha,$$

and the strips T_α are *generators* for S, i.e., any strip T_α may be obtained from any other by a rotation about the axis of S. Suppose the elements $S_{\alpha\beta}$ are ordered as follows:

$$S_{11}, S_{12}, \ldots, S_{1,n_e}, S_{21}, S_{22}, \ldots, S_{2,n_e}, \ldots, S_{n_s,1}, S_{n_s,2}, \ldots, S_{n_s,n_e}.$$

Then the matrices $\hat{L}$, $\hat{M}$, $\hat{M}^{\mathrm{T}}$ and $\hat{N}$ will each have a *block circulant* structure. For example, if $n_s = 4$, then

$$\hat{L} = \begin{bmatrix} C_0 & C_3 & C_2 & C_1 \\ C_1 & C_0 & C_3 & C_2 \\ C_2 & C_1 & C_0 & C_3 \\ C_3 & C_2 & C_1 & C_0 \end{bmatrix},$$

where C_i is a $n_e \times n_e$ sub-matrix. To store $\hat{L}$ it is only necessary to store the sub-matrices C_i, $i = 0, \ldots, 3$, and, furthermore, we can solve algebraic equations involving (block) circulant matrices using algorithms based on the Fast Fourier Transform (FFT) that are very efficient [34].

It can be shown that if the matrix C has a circulant structure generated by a set of elements $\mathbf{c} = (c_0, c_1, \ldots, c_{n-1})^{\mathrm{T}}$, and F_n denotes the Discrete Fourier Transform (DFT) matrix of order n, then solving the system of equations

$$C(\mathbf{c})\mathbf{x} = F_n^{-1}\mathrm{diag}(F_n\mathbf{c})F_n\mathbf{x} = \mathbf{y}$$

can be achieved by carrying out the following operations:

1. apply a DFT to $\mathbf{y}$,
2. multiply the result of 1 by the inverse of a diagonal matrix whose elements are obtained by applying a DFT to $\mathbf{c}$, and
3. apply an inverse DFT to the result of 2.

A similar method can be applied to problems involving *block* circulant matrices such as those that arise in the BEM application.

4. SOFTWARE IMPLEMENTATION

This Section describes the software packages that have been used for the near to far field calculations. One package is an implementation of the Burton-Miller method, as outlined in Section 3.1.4.2, and the other is an implementation of the CHIEF method, as outlined in Section 3.1.4.1. Section 4.1 describes the two packages, and explains some of the issues encountered when they were used at NPL.

If the user is to have confidence in the results delivered by software, the software must be shown to be fit for purpose, and there needs to be documented evidence of this. Prior to applying the two packages to real measurement data, they were tested using several sets of data. The test problems and results are described in Section 4.2. In addition, the packages have been tested as part of the "Testing Continuous Modelling Software" project funded as part of the DTI National Metrology System Directorate Software Support for Metrology (SS*f*M) programme [36,37]. The results of this work are briefly presented in Section 4.2.3.

4.1 SOFTWARE PACKAGES

There is a wide choice of software packages available for solving boundary element problems, ranging from proprietary packages to freeware designed for the solution of a particular problem. The choice of packages described here was mainly motivated by two factors. The software was chosen with acoustics, and particularly underwater acoustics, problems in mind. Both packages we have used are designed for applications in acoustics and so they formulate the problems and inputs in a way that is familiar to experts in the field. The second factor was the work reported by Meyer *et al* [10] that suggested that the Burton-Miller method was more straightforward to implement than some of the alternatives. This paper led us to look for a solution using the Burton-Miller method.

As well as the software described in this Section, we also use PAFEC (originally a finite element code) for vibroacoustic calculations. PAFEC includes an implementation of the CHIEF and Burton-Miller methods and can solve two and three-dimensional problems for general and axisymmetric geometries.

4.1.1 The Burton-Miller software of Kirkup

Kirkup's software is an implementation of the Burton-Miller method, available from http://www.soundsoft.demon.co.uk/. The software can be used for interior or exterior problems, and can solve problems in two or three dimensions, including a two-dimensional formulation of problems with axisymmetry of the geometry and the boundary conditions. In addition, the software includes extra routines for solution of the interior eigenvalue problem that determines the resonance frequencies of a given geometry. Such routines are useful for identifying the wavenumbers that cause Equation (3.10) to become ill-conditioned.

The software is available as Fortran source code. The code is fully commented, and the documentation [31] describes the theory underlying all the routines and provides examples of the code being used. The code includes checks that the inputs are valid, including checks that the element sizes and shapes are within acceptable limits, the surface is closed, and the surface definition is oriented correctly. These routines can be very helpful when troubleshooting.

The software requires the user to define a mesh by supplying nodal coordinates and the connectivity of the elements joining the nodes. The element type depends on the problem being solved. In two dimensions the elements are straight lines, in three dimensions they are planar triangles, and in axisymmetric problems they are straight lines representing truncated conic shells. The element connectivity must be defined such that the surface normal is pointing outwards. The points in the domain at which the solution is required are defined by specifying their coordinates.

The software accepts general Robin boundary conditions of the form given in Equation (3.5), but because the experimental procedure measures pressure we have used Dirichlet conditions as in Equation (3.3). The software also allows the user to define an incident velocity potential on the surface and at the domain points where the solution is required, for problems involving a scattering of a field with a specified incident velocity potential.

The software requires values for f, the frequency, ρ, the density of the fluid, and c, the speed of sound in the fluid. The other quantity that affects the results is the coupling coefficient μ. This is defined within the source code to be $i/(k + 1)$, where k is the wavenumber, but can easily be altered. Alternative choices of μ are discussed in Section 4.2.

4.1.2 The CHIEF software of Forsythe

Forsythe's Matlab realisation of CHIEF is a boundary element solver that uses the CHIEF method for external Helmholtz problems. The software itself is also known as CHIEF. The version of CHIEF for Matlab that was used in this study was developed by S.E Forsythe of the United States' Naval Undersea Warfare Center, Newport, Rhode Island, USA [38]. Forsythe makes the Matlab version of the code available to interested parties in the form of a suite of Matlab m-files and he can be contacted by e-mail at seforsythe@npt.nuwc.navy.mil.

The software is designed to solve underwater acoustic problems in three-dimensional space and does not have a special formulation for axisymmetric problems. Instead, it exploits circulant matrix methods, as described in Section 3.2.2, to handle problems involving surfaces that have rotational or reflective symmetry efficiently. As well as solving problems with Robin conditions as in Equation (3.5), the software can solve problems involving two regions of the domain with different properties (density and sound speed) where the conditions require continuity of pressure and velocity at the boundary between the two regions.

The majority of the code is in the form of Matlab M-files, although some of the routines are within a compiled library, and so the majority of the source code is available. The routines do not check for distortion, closure, or orientation. Sample files for well-understood problems are supplied to demonstrate usage of the software. The documentation describes the theory behind the code and outlines the key features of the software.

The mesh can be defined in two different ways. The direct approach is to define a set of nodes and a connectivity for each of the elements. The elements are all 8-noded quadrilaterals and they do not need to be flat. Triangular elements can be defined if necessary by defining a degenerate element connectivity. The alternative to this is to use some of the many patch definition and manipulation commands supplied with the software. A patch is defined as any shape that can be mapped onto a rectangle in the (u, v) plane. The patch commands can generate patches on generic surfaces such as spheres, cylinders, planes etc. The manipulation commands can join the patches together to generate a closed surface mesh. The mesh is still defined by a set of nodal coordinates and connectivity, but the user does not have to supply these directly.

As was mentioned above, CHIEF makes good use of symmetrical geometries to reduce its CPU and memory requirements. As a result, the best way of defining a symmetric domain is to define the generator of the symmetry and the order of rotational symmetry. The generator of the symmetry is a representative strip that is rotated around some axis to produce the full geometry. The order of rotational symmetry is the number of rotated copies of the generator that are required to make up the full geometry. Figure 4.1 shows an example of a generator, in this case a Section of an approximation to a closed cylinder. The original cylinder was of radius 0.1 m and height 0.5 m, and the wavelength that defined the mesh size led to an order of rotational symmetry of 64 and a maximum element dimension of approximately 10 mm.

The software uses Fast Fourier Transform (FFT) methods to speed up the execution. The use of FFT methods means that a computational advantage can be gained if the order of rotational symmetry is a product of small primes (e.g. 32, 48, 60 rather than 31, 47 or 61). The software has been developed to pick the smallest product of small primes that produces a sufficiently small element size.

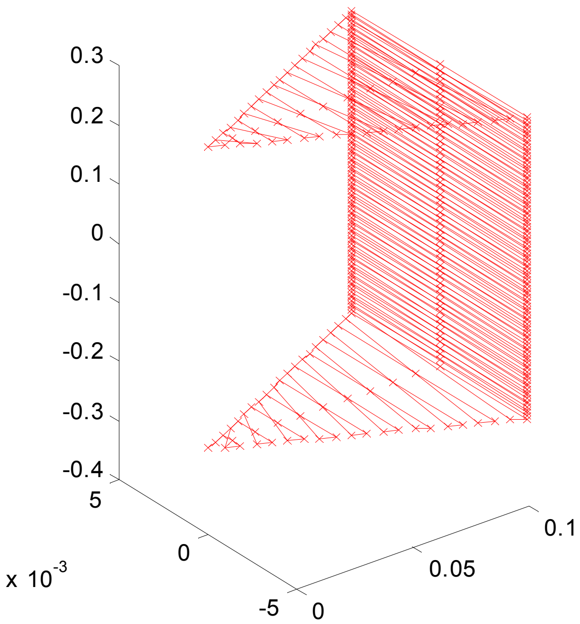

Figure 4.1 Nodes from a representative slice of a cylinder with order of rotational symmetry 64.

Boundary conditions can be defined as generalised Robin conditions on the closed surface, or if the conditions on the surface are generated by source points at known locations in the domain they can be calculated by CHIEF. If the problem involves multiple regions of the domain with different properties, the software can impose continuity conditions on the pressure or the velocity between regions.

The software requires values for f, the frequency, ρ, the density of the fluid, and c, the speed of sound in the fluid. If the problem is likely to have uniqueness problems as described in Section 3.1.4, then interior points must be specified where the condition of Equation (3.15) can be applied. We are not aware of any methodology for selecting the location or number of these points, but it is known that the problem will be ill-conditioned if the points are located at the nodes of the interior resonance problem described in Section 3.1.4.

An important point to note is that Forsythe's version of CHIEF defines the Green's function as

$$G(\mathbf{p},\mathbf{q}) = \frac{e^{-ik\|\mathbf{p}-\mathbf{q}\|}}{4\pi\|\mathbf{p}-\mathbf{q}\|} \qquad (4.1)$$

instead of the form stated in Section 3.1.1. The two forms are complex conjugates. The form in Equation (4.1) does not obey the Sommerfeld radiation condition of Equation (3.7), instead it obeys

$$\lim_{r\to\infty} r\left(\frac{\partial\varphi}{\partial r} + ik\varphi\right) = 0,$$

which is quoted as the Sommerfeld radiation condition in the accompanying documentation. The main effect of this difference is that care must be taken when using the software as it is necessary to use the complex conjugate of the measurement value for the boundary conditions.

4.1.3 Implementation issues

We explained in Section 3.1.4 that the Burton-Miller and CHIEF methods use different methods to avoid the non-uniqueness problems that occur when the boundary element method is used to solve the Helmholtz equation. Both methods require the definition of extra inputs before the solution can proceed. The Burton-Miller method requires the definition of a coupling coefficient μ, and the CHIEF method requires the definition of internal points.

Some work [31, 39-40] has been done on choosing a good value for μ. As stated in Section 3.1.4.2, it can be shown that the formulation (3.17) has a unique solution provided that μ has a non-zero imaginary part. Kirkup [31] recommends using $\mu = i / (k + 1)$, as stated in Section 4.1.1. This value is chosen by considering the relative sizes of the terms in (3.28),

$$\left(-\frac{1}{2}\hat{I} + \hat{M} + \mu\hat{N}\right)\mathbf{u} = \left[\hat{L} + \mu\left(\frac{1}{2}\hat{I} + \hat{M}^{\mathrm{T}}\right)\right]\mathbf{v},$$

and choosing μ so that

$$\mu\left\|\hat{N}\right\| \approx \left\|-\frac{1}{2}I + \hat{M}\right\|, \quad \text{and}$$

$$\left\|\hat{L}\right\| \approx \mu\left\|-\frac{1}{2}I + \hat{M}^T\right\|,$$

for a suitable norm, so that the operators are balanced and the problem remains well-conditioned. Such an analysis shows that $\mu \sim 1/k$ will balance the operators, and using $\mu = i / (k + 1)$ ensures that μ will always be finite and will have a non-zero imaginary part. An alternative to this is to calculate the terms in the matrices and then define

$$\mu \approx \left\|-\frac{1}{2}I + \hat{M}\right\| \Big/ \left\|\hat{N}\right\|, \quad \text{or}$$

$$\mu \approx \left\|\hat{L}\right\| \Big/ \left\|-\frac{1}{2}I + \hat{M}^T\right\|.$$

There is little guidance available on choosing locations of internal points for use with the CHIEF method. The only requirement is that the points should not be located at the nodes of the fundamental mode of the closed surface. Previous work [37] has used randomly generated locations successfully. However, as the frequency increases, the nodes of the associated normal mode will become more numerous and so it will become more likely that a randomly-generated point will be a node. It is not known at present whether the quality of the solution deteriorates when the CHIEF point is close to a node. It is worth investigating these issues further.

The main factor that determines the computational effort involved in calculating a solution is the size of the matrices involved. The size of the matrices is determined by the number of elements used to mesh the surface. The number of elements used is determined by the maximum element size that produces convergent results (given by $\lambda/3$). It may be necessary to interpolate the measured data onto the mesh if the measurement points do not coincide with the points where the mesh requires data.

If the Fourier component method described in Section 3.1.5 is to be used, the user needs to decide how many Fourier components are required. A balance needs to be struck between adequate approximation of the input data and using few enough components that the advantages gained by using the method are not cancelled out by the cost of running the software repeatedly for each Fourier component.

As was explained in Section 3.1.5, the calculations for the individual Fourier components are independent of one another. This independence means that the calculations for different components can be carried out on separate computers without any communication between the computers being necessary. This makes the problem ideal for solution using a distributed computing network. The majority of the results generated using the Burton-Miller method were calculated using NPL's distributed computing network. The distributed computing network solved in hours problems that would have taken days to solve using a single desktop PC. A good practice guide on distributed computing is currently being developed as part of the third DTI NMS SS*f*M programme, and will be available from the SS*f*M website in 2006.

4.2 SOFTWARE TESTING

The software implementations are tested using two different analytical solutions to the Helmholtz Equation (3.2). The axisymmetric version of the Burton-Miller software is used in the tests as that is what would be used to process experimental data. The analytic solutions used are the field generated by a point source located at the origin, which in this case is a scaled version of the Green's function and has the form

$$p(r) = \frac{e^{\pm ikr}}{2\pi r}$$

where r is the distance from the source to a point in the domain, and the field generated by a dipole, which has the form

$$p(r,x) = D\frac{\rho ck^2}{4\pi}\frac{e^{\pm ikr}}{r}\left(\pm ik - \frac{1}{r}\right)\frac{x}{r}$$

where D is a small constant (10^{-6} in the test cases) and x is the Cartesian x coordinate of the point in the domain. The dipole is equivalent to two point sources, 180º out of phase, separated by a distance D in the x direction. The ± sign is used because CHIEF and Burton-Miller software use different Green's functions. The plus applies to the Burton-Miller software and the minus to CHIEF. The surface S was a cylinder of radius 0.1 and height 0.5, centred at the origin. No units have been specified throughout since the software is not bound to any one set of units.

Throughout the tests, the sound speed and density were held fixed at 1461 and 1000 respectively. Ten frequencies were used for the tests, between 500 and 5000 at intervals of 500. A different mesh was used for each frequency, with the element size being chosen such that good results should be obtained. Approximately the same mesh size was used for the two packages so that the two sets of results should have been about the same quality.

For each test, the exterior problem was solved at the points

$$(x,y,z) = \begin{cases} \left(1 + {}^{j}\!/_{20}, 0, 0\right), & j = 0,1,\ldots,200, \\ \left(10^m, 0, 0\right), & m = 2,3,\ldots,6, \\ \left(5\times 10^n, 0, 0\right), & n = 1,2,\ldots,5, \end{cases}$$

making 211 output points in total. The final 10 points were included in order to assess the packages' ability to calculate the extreme far-field behaviour and the results obtained at these points will be discussed separately.

4.2.1 Test results in the mid to far field

This section discusses the software results obtained for $(x, y, z) = (1 + {}^{j}/_{20}, 0, 0)$, $j = 0, 1, \ldots, 200$. Two typical sets of results are shown in Figures 4.2 and 4.3. Figure 4.2 shows the real and imaginary values, calculated from the analytic formula and by the CHIEF and Burton-

Miller packages, for a point source with f = 500. Figure 4.3 shows the corresponding results for a dipole with f = 500.

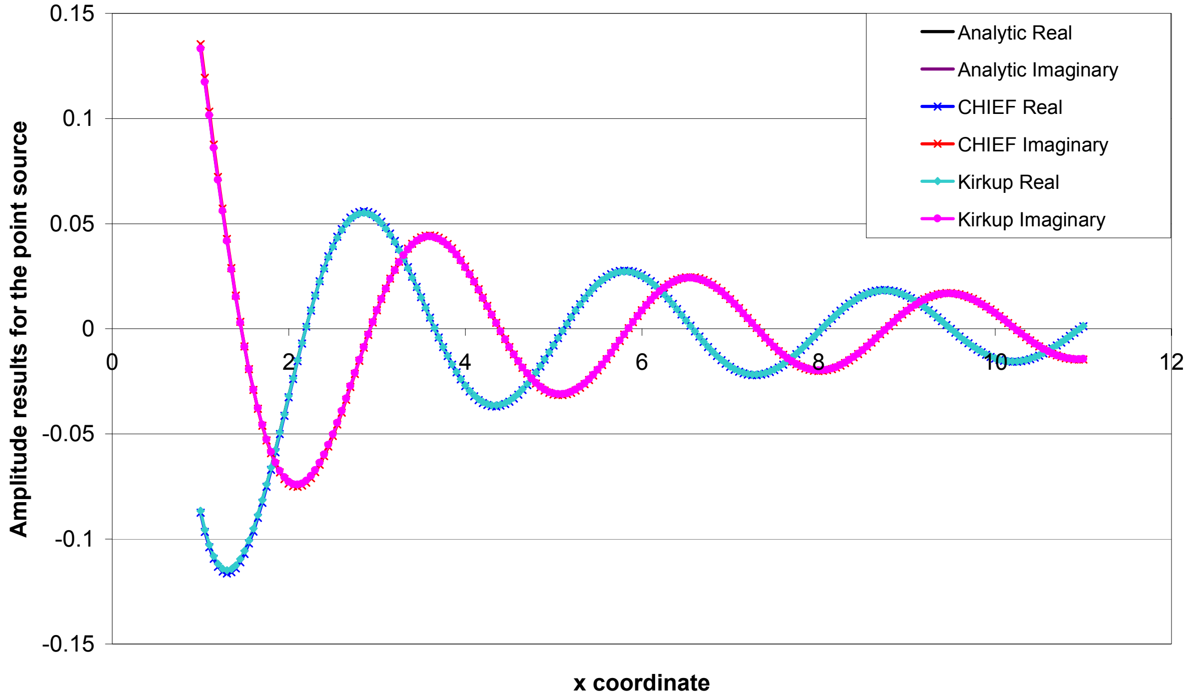

Figure 4.2 Real and imaginary example results for the point source test. The software results and the analytic solution overlie one another.

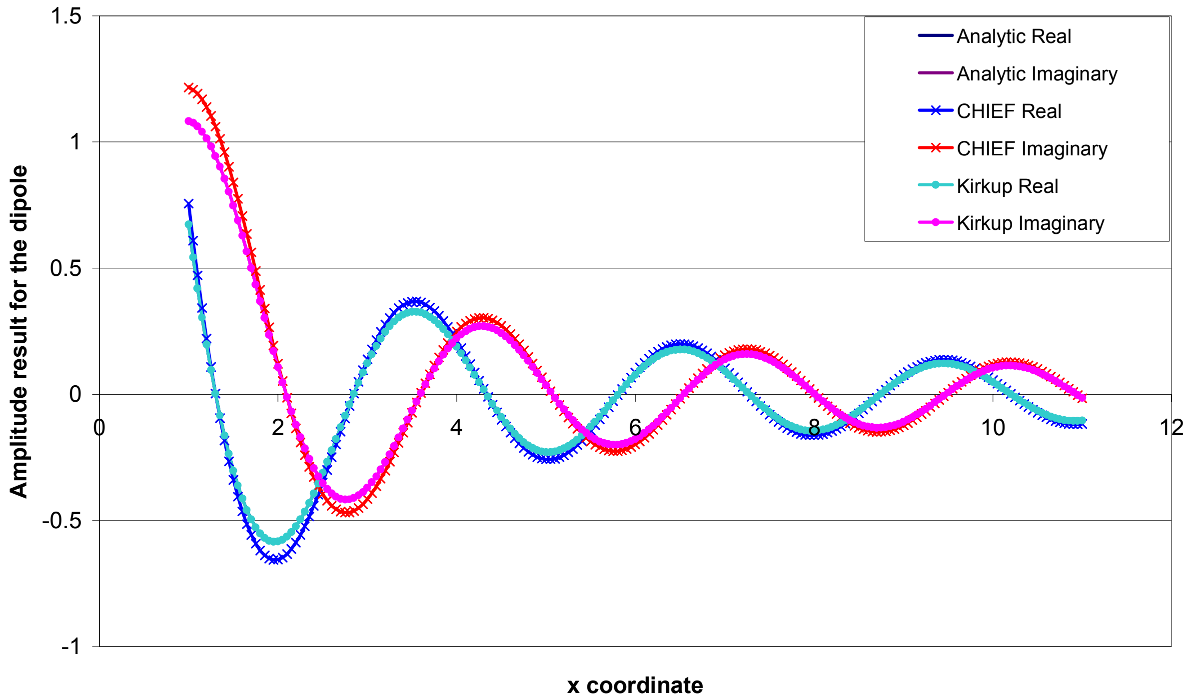

Figure 4.3 Real and imaginary example results for the dipole test. The results of the Burton-Miller software and the analytic solution overlie one another.

It is clear from Figures 4.2 and 4.3 that both software packages give excellent agreement for the point source and good agreement for the dipole for f = 500. It is not currently clear why the results of the Burton-Miller software are better than those of the CHIEF software for the frequency shown.

Previous work on software testing (for example [41] and [36]) has recommended the use of a performance metric to describe the numerical performance of software in tests. One metric that is suitable for the results of these tests is

$$N(\mathbf{x}) = \begin{cases} \min\left\{ M(\mathbf{x}), \log_{10}\left(1 + \dfrac{RMS(\mathbf{y}_{\text{ref}}(\mathbf{x}))}{RMS(\mathbf{y}_{\text{ref}}(\mathbf{x}) - \mathbf{y}_{\text{test}}(\mathbf{x}))} \right) \right\} & RMS(\mathbf{y}_{\text{ref}}(\mathbf{x}) - \mathbf{y}_{\text{test}}(\mathbf{x})) > 0 \\ M(\mathbf{x}) & RMS(\mathbf{y}_{\text{ref}}(\mathbf{x}) - \mathbf{y}_{\text{test}}(\mathbf{x})) = 0 \end{cases}$$

where $\mathbf{y}_{\text{ref}}(\mathbf{x})$ is the set of reference results (in this case the analytic solution), $\mathbf{y}_{\text{test}}(\mathbf{x})$ is the corresponding set of results calculated by the software being tested, and $M(\mathbf{x})$ is the number of correct significant figures in the reference results $\mathbf{y}_{\text{ref}}$. N measures the number of figures of agreement between the reference result and the test result, and so the larger the value of N, the better the software has performed. The quantity has been calculated for the test results in two ways: as a function of position, and as a single value for each set of results. Figure 4.4 shows a typical variation of N with position. The values shown were calculated by comparing the real part of the results of the software packages to the analytic solution for the point source at f = 500. Also shown is the reference solution to the problem, plotted on the secondary axis.

Further examination shows that for both software packages,

$$y_{\text{ref}}(x) - y_{\text{test}}(x) \approx \frac{\varepsilon e^{i(kx-\gamma)}}{x},$$

where ε and γ depend on the package used. For the Burton-Miller software, $\gamma \approx \pi$ and so the maximum difference between the test and reference results should occur at approximately the same value of x as the maxima and minima of the reference solution. This prediction agrees with the results shown in Figure 4.4.

Figure 4.5 shows the calculated value of N for the tests at different frequencies obtained by treating each set of results as a single set and ignoring the dependence on position. The difference in performance of the two packages is likely to be due to the use of the axisymmetric option of the Burton-Miller software. The use of a two-dimensional model may reduce the effects of discretisation on the results, thus making them more accurate than the equivalent three-dimensional results. A possible test of this would be to run an equivalent three-dimensional model using the Burton-Miller software for comparison, but this has not been done.

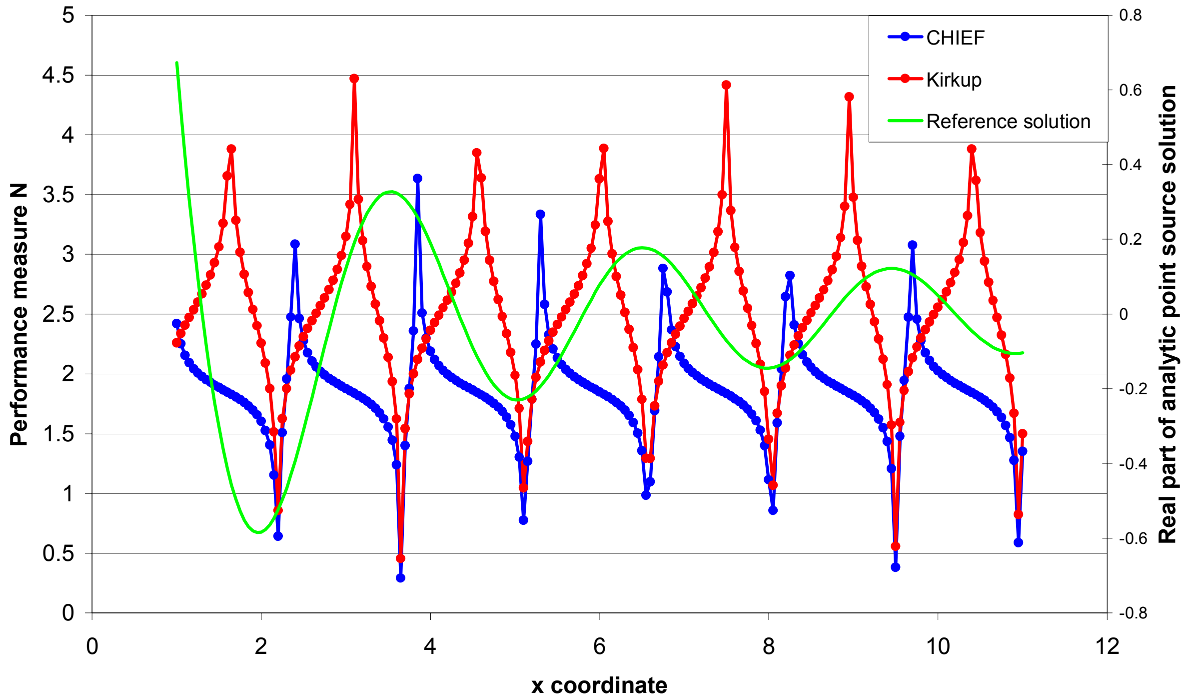

Figure 4.4 Performance measure plotted against position for the point source.

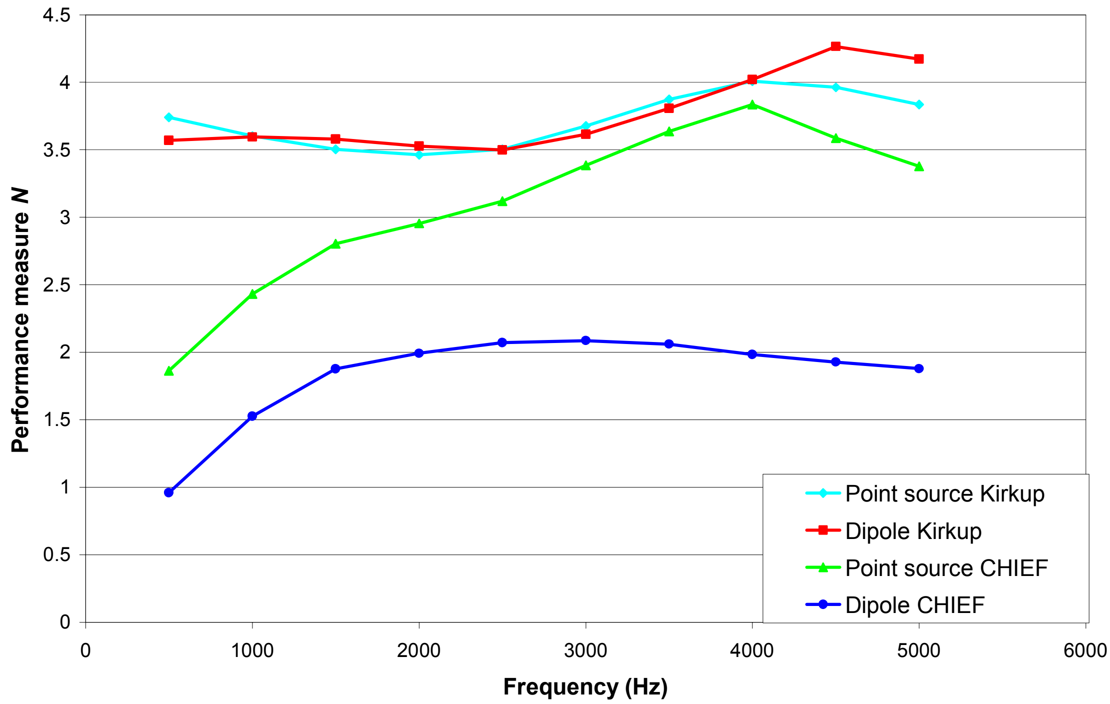

Figure 4.5 Performance measure plotted against frequency for both tests and both software packages.

4.2.2 Test results in the far field

The far-field behaviour of the results of the two packages differed markedly. Typical results are shown in Figures 4.6 and 4.7. These figures show the performance measure from the point source test, plotted against the logarithm of the x coordinate of the far field point for the different frequencies. Figure 4.6 shows the results from The Burton-Miller software, and Figure 4.7 shows the results of the CHIEF software.

The main difference between these two figures is the manner in which the quality of the results decreases as the distance from the source increases. The Burton-Miller software shows a gradual decrease in the quality of the results, with all frequencies exhibiting roughly the same trend ($N \sim x^{-0.4}$ as $x \rightarrow \infty$). The CHIEF software shows an approximately constant value of the performance measure for a given frequency until the results suddenly become very poor (no figures of agreement between test results and the reference results) at some distance. The results of the CHIEF software jumped in magnitude from about 10^{-5} to about 10^{10} when this drop in quality occurred.

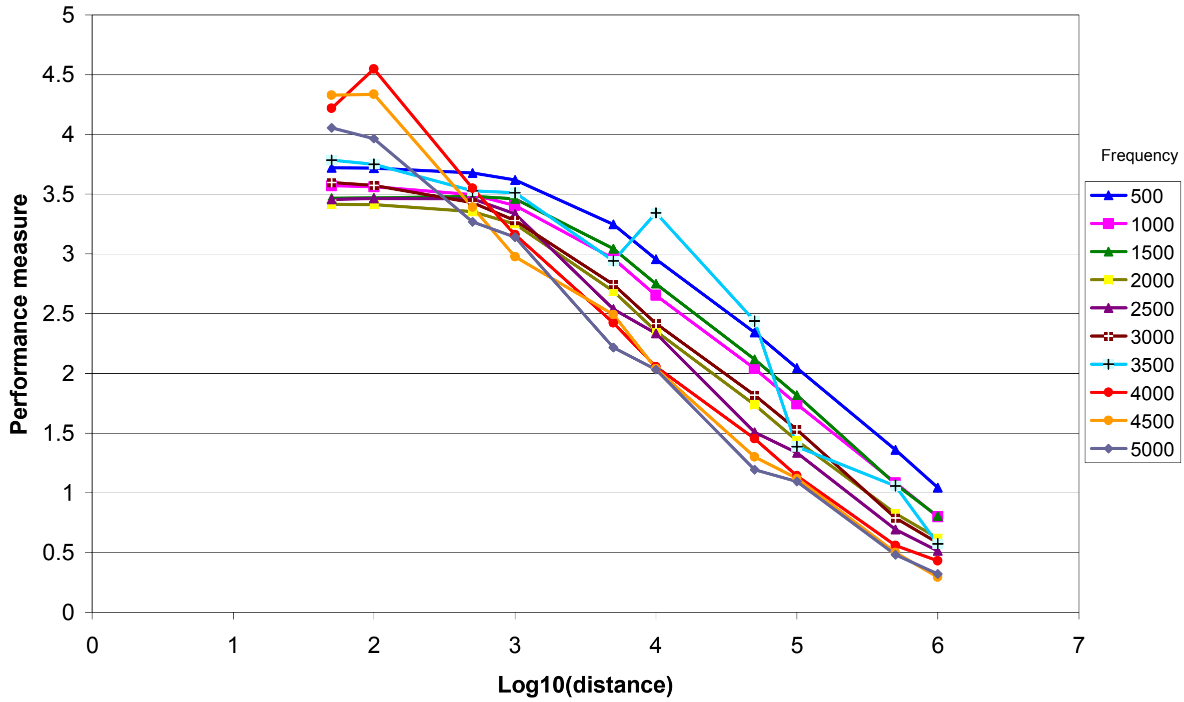

Figure 4.6 Performance measure of the far-field results for the point source calculated using The Burton-Miller software.

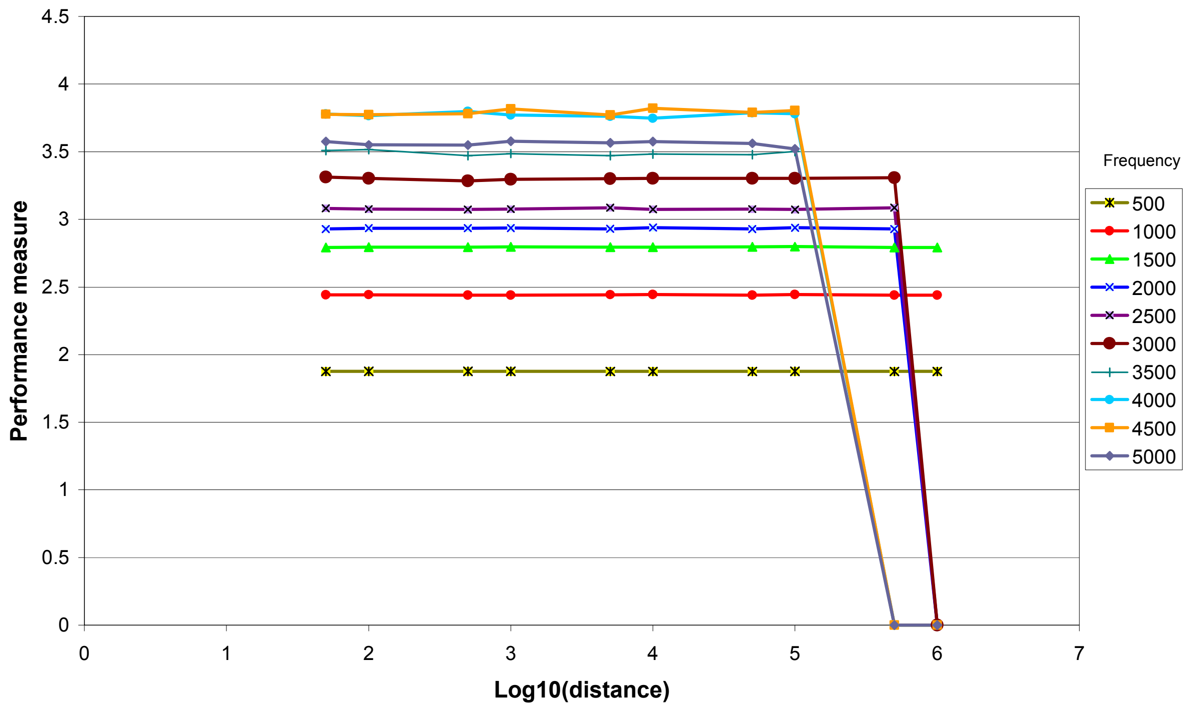

Figure 4.7 Performance measure of the far-field results for the point source calculated using the CHIEF software

Once the solution on the surface S is known, the solution in the far field requires calculation of the integrals

$$\int_{e_j} G_k(\mathbf{p}, \mathbf{q}_j)\, dS_{q_j}, \quad j = 1, 2, \ldots, N_e, \quad \text{and} \quad \int_{e_j} \frac{\partial G_k(\mathbf{p}, \mathbf{q}_j)}{\partial n_{q_j}}\, dS_{q_j}, \quad j = 1, 2, \ldots, N_e,$$

where e_j is a boundary element, N_e is the total number of boundary elements, and $\mathbf{p}$ is the far-field point of interest. As $\mathbf{p} \to \infty$, these integrals become more difficult to calculate accurately, and this will incrementally and adversely affect the quality of the solutions. This may be the cause of the gradual decline of accuracy shown by The Burton-Miller software.

Further examination of the CHIEF results showed that for large values of x, the results became extremely large (typically of the order of 10^{14} times the analytic result). This behaviour may be caused by an overflow error, so for instance the software may have tried to calculate e^x for too large a value of x. Further investigation of the behaviour of these test results is required. It is possible that the poor behaviour only occurs at distances that would not be considered in real applications of the software. It would also be useful to investigate why the results of the two software packages behave so differently as $\mathbf{p} \to \infty$.

4.2.3 Other tests of these software packages

As was mentioned at the start of this Section, another set of tests has been carried out on the two software packages used in this work (see [37]). The results will not be quoted in full here, but a summary of the results is shown in Table 4.1.

The test problem was calculation of the far-field produced by a point source irradiating a rigid sphere in water. Two frequencies were chosen; one for which non-uniqueness would not be a problem, and the other (750 Hz, an eigenfrequency of the sphere in this case) where it would be a problem. The reference results used for comparison were generated using a finite element package, PAFEC, which offers several independent methods for solving such problems. The results chosen were the pressure amplitudes at 181 points around a semi-circle of large radius.

Software details	Frequency (Hz)	
	238.7	750
Burton-Miller	1.33	1.61
CHIEF, no internal points	2.88	0.47
CHIEF, internal points	2.88	2.49

Table 4.1 Values of *N*, the performance measure, for the various sets of test results.

The difference in performance between the Burton-Miller software and CHIEF may be caused by the differences in the meshes used for the two tests. The main point to note from table 4.1 is the behaviour of CHIEF with and without the internal points. At the frequency that has no non-uniqueness problems, CHIEF produces the same performance whether internal points are used or not. A detailed comparison of the two sets of results from CHIEF shows that the two sets of results agree up to the sixth decimal place. However, for the frequency where non-uniqueness is a problem, the results generated without using internal points are significantly worse than those generated using internal points. An example is shown in Figure 4.8. This figure shows the pressure amplitude plotted against an angular coordinate for the reference results and the three sets of test results.

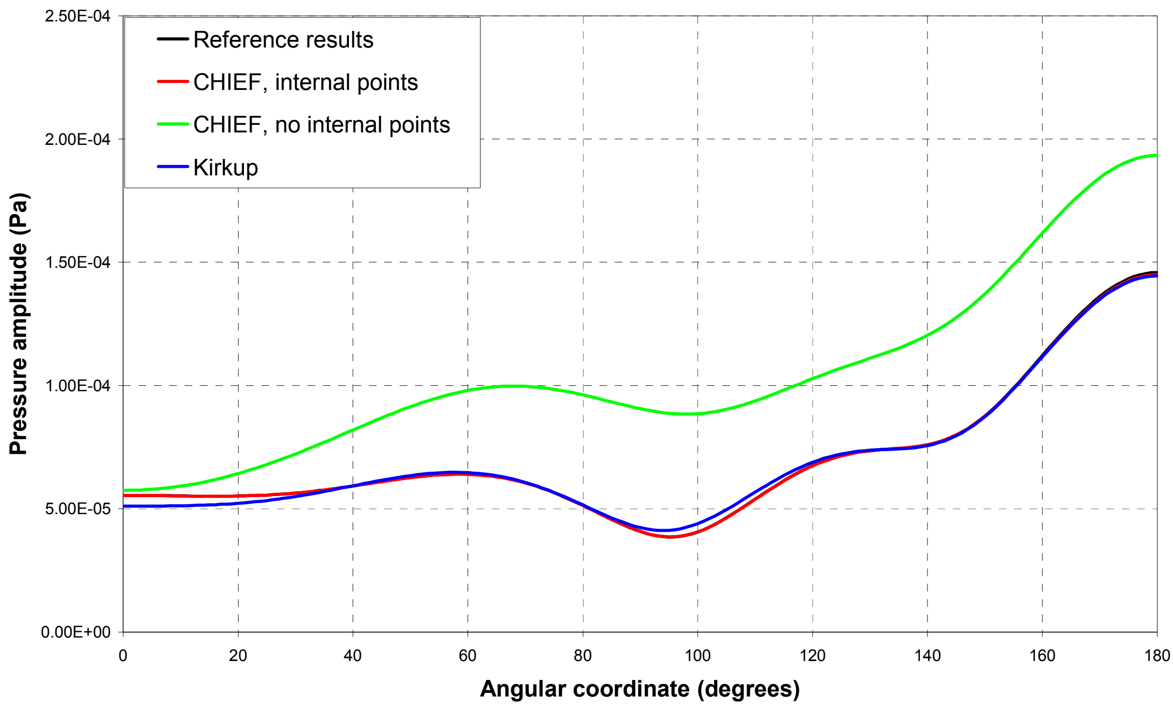

Figure 4.8 Results of a test involving a non-uniqueness problem (fill details of test given in [37]). The reference results underlie the CHIEF results with internal points.

The results in Figure 4.8 that were produced without using internal points consistently are of higher magnitude than those produced using The Burton-Miller software and those produced using internal points. This illustrates the effects that the non-uniqueness problem can produce. It is interesting to note that the bad results are not obviously bad: they are continuous, smooth, and of a reasonable size. If reference results were not available it would be easy to think that these results were correct. Since the use of internal points does not adversely affect the quality of the results when the points are not necessary, it is worth using internal points for all cases unless this will adversely affect the computational effort.

5. EXPERIMENTAL MEASUREMENTS

5.1 MEASUREMENT FACILITY

The measurements described in this report were made using the large Open Tank Facility at NPL. This consists of a cylindrical wooden test tank of dimensions 5 m deep and 5.5 m in diameter filled with fresh water. The facility is equipped with a high-precision positioning system consisting of vibration-isolated beams supporting three positioning carriages. Two of the carriages have three orthogonal degrees of freedom in translation (X, Y and Z) and one rotational degree of freedom about a vertical axis (θ_Z). The other carriage has only one vertical degree of freedom in translation along with the rotational degree of freedom, but can handle heavier loads of up to 50 kg in-air weight (compared to 20 kg for the *XYZ* carriages). Remote computer control of all carriages is available including simultaneous movement of all axes. The maximum travel under computer control in translation is 1 m, with a linear resolution of 5 μm, but extended travel is available in the X direction by rolling the carriages along the precision rails mounted on the beams and locating in one of the preset locking positions, which are 250 mm apart. The angular resolution in rotation is 0.005°. Figure 5.1 shows a photograph of facility with the positioning carriages clearly visible.

Figure 5.1 Photograph of the NPL large Open Tank Facility showing the carriages of the positioning system

The transducers used in the test tank are suspended from mounting poles that are screwed into the rotary stages of the positioning system such that the axis of rotation is coincident with the axis of the mounting poles. Two types of mounting pole are used to attach the transducers to the positioning system. The first connects directly to the rotary stages and is made from 80 mm diameter free-flooding carbon fibre tube of length 2.4 m. The second attaches to the end of the first pole, is made of 16 mm diameter free-flooding carbon fibre tube, and is approximately 1 m in length, the exact length depending on the type of transducer fitting mounted on the end. A range of these narrower poles are available with different transducer fittings, each shaped to accept the body of a specific hydrophone or transducer that is in common use. Carbon fibre was used as a material for the poles because it is lighter than an equivalent metal pole, possesses great strength and stiffness, is easy to manufacture in tubular sections which are straight to a high degree of accuracy, and does not have the problems with corrosion associated with metal fixtures submerged in water. This system of transducer mounting enables precise positioning of acoustic transducers at a range of positions within the tank. The typical depth used for acoustic testing is 2.5 m since this allows maximum echo-free time before the arrival of reflections from the tank boundaries and the water surface. The poles can be seen mounted on the carriages in the photograph of Figure 5.1, and Figure 5.2 shows a schematic diagram of the entire Open Tank Facility.

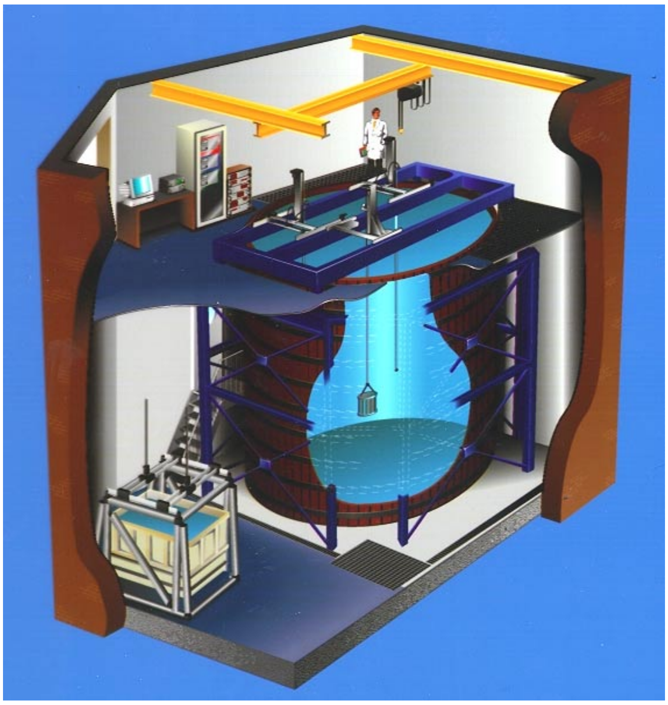

Figure 5.2 Schematic diagram of the NPL Open Tank Facilities.

The scans are undertaken under computer control with measurements made at discrete intervals. Scans are also possible "on-the-fly" while the carriages are continuously moving, but this mode of operation was not used for the measurements reported here. For each measurement, the hydrophone signal is digitised using an HP89410A vector signal analyser, which can sample the waveform at rates of up to 25.6 megasamples per second (the analyser providing a usable bandwidth of 10 MHz). The resolution of the ADC is enhanced by dithered signal processing to provide up to 23 effective bits. Both the magnitude and the phase of the signal may be measured, either using on-board analysis based on fast Fourier transforms, or by first transferring the waveform to the computer and performing analysis in software. The software used to measure the signal uses either a discrete Fourier transform algorithm, or one based on fitting a sinusoidal waveform to the signal using a least squares technique. A separate data file is stored containing the results for each circular data set including the magnitude and phase of the signal for each of the discrete angular steps, and the depths of the transducers.

A range of electronic instrumentation is available for use in the measurements. These include power amplifiers for use in transmission, hydrophone preamplifiers to boost the received signal, and programmable filters to condition the signal.

To measure on a cylindrical surface surrounding the projecting transducer, a series of measurements is made on concentric circles of the same radius but offset in depth. Each circular data set is obtained by rotating the projector and not by scanning the hydrophone, as depicted in Figure 5.3. In between the measurement of each successive circular data set, the depth of the projector and/or hydrophone is adjusted so that the next data set is measured with the relative depth increased by a specified increment.

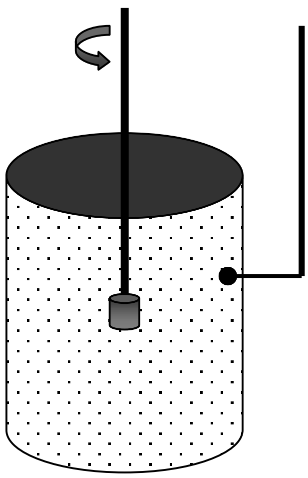

Figure 5.3 Schematic representation of a cylindrical scan.

A smaller tank is also available for high frequency work, consisting of a 2 m x 1.5 m x 1.5 m GRP tank with a two-carriage positioning system. Both carriages have three orthogonal degrees of freedom in translation (*X*, *Y* and *Z*) and one rotational degree of freedom about a vertical axis (θ_Z) with 10 µm linear resolution and 0.01° angular resolution. It also features a glass window to allow optical interrogation of the acoustic field. This facility was not used for the work reported here, but is also shown in the schematic diagram of Figure 5.2.

5.2 DESIGN OF TEST ARRAY

To exercise the method, a source was required upon which measurements could be attempted. It was considered that the source should have some interesting features in its directional response rather than being nominally omnidirectional, since it would then be possible to test the ability of the method to reproduce the features in the predicted response. However, the source would ideally be small enough so that within the same tank, measurements are also possible in the acoustic far-field to validate the method. In addition, it should be remembered that a source of too high a frequency would be so directional that cylindrical measurement surfaces would not be an appropriate choice of measurement geometry (instead, the planar measurement geometries used in Fourier-based near-field techniques would be better suited).

Since no suitable source was available to NPL off the shelf, a special source was constructed for the purposes of this work. This consisted of two free-flooding cylindrical piezoelectric projectors. Each cylinder was 98 mm in diameter and 90 mm long and encapsulated in polyurethane. The cylinders had resonance frequencies at both 13.9 kHz and 27.5 kHz (these were the frequencies where the transmitting voltage response reached a local maximum).

The transducers were mounted in a couple of different configurations to provide two different sources. In the first configuration, the transducers were simply mounted co-axially, one above the other, as shown schematically in Figure 5.4 (left hand diagram). With both transducers driven in phase, this provided some directionality in the vertical orientation with a maximum output in the far-field produced in an orthogonal plane passing through the mid-point of the source (the plane bisecting the two transducers). This configuration was given the name "DUAL".

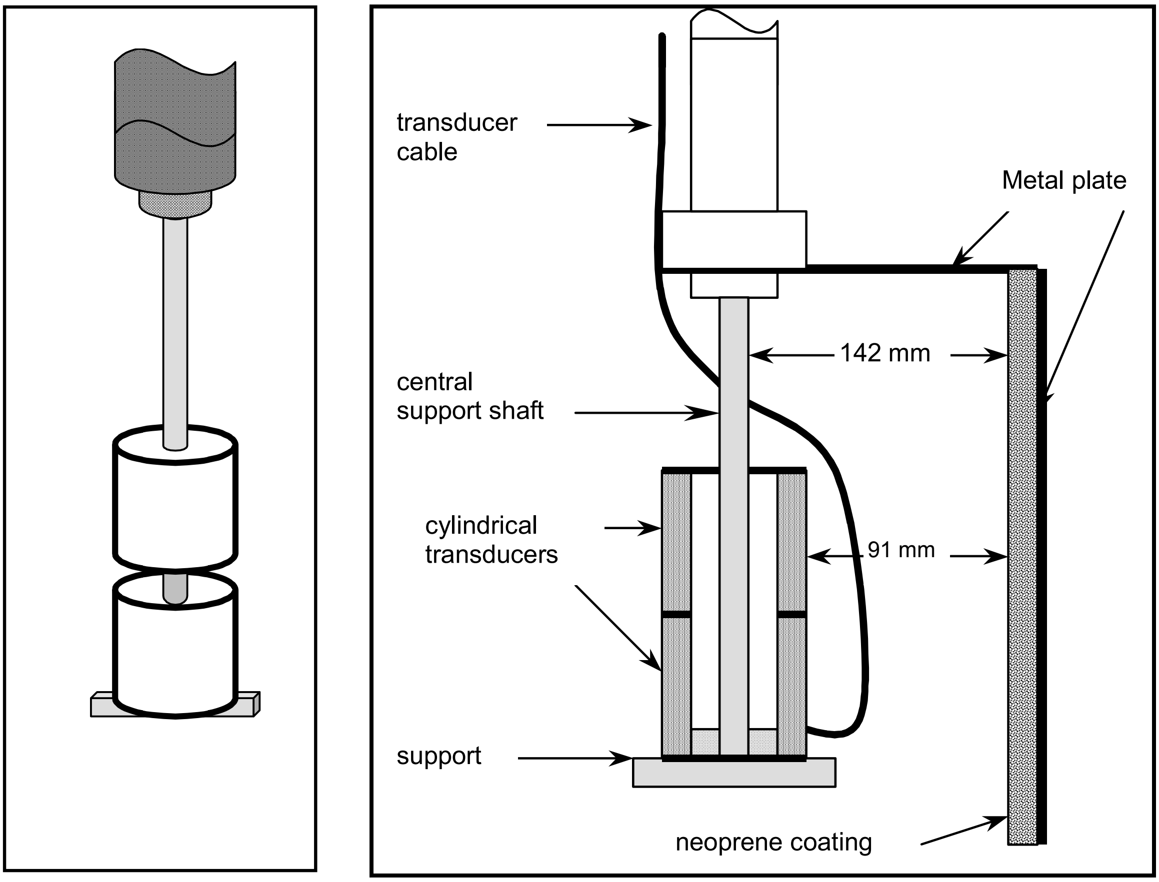

Figure 5.4 Schematic diagram of the two transducer configurations. Left: the DUAL configuration. Right: a side view of the DUREF configuration showing the neoprene-coated steel plate used as a reflector (not to scale).

To provide some directionality in the azimuth direction, a reflector was positioned close to the pair of transducers to create sufficient interference between the reflected and directly radiated fields to produce lobes in the azimuth direction in the far-field response. Figure 5.4 shows a side elevation of the arrangement (right hand diagram). The reflector was made from a thin steel plate that was coated on the inner surface with a 3 mm thick layer of closed-cell neoprene rubber (similar to "wet-suit rubber"). The air-filled cavities within the neoprene ensured that a strong reflection was obtained, producing significant interference and well-defined lobes. Use of the steel plate alone did not provide a strong reflection for sound at 13.9 kHz (where the wavelength is 53 mm). To distinguish this arrangement from the configuration without the reflector, this was named “DUREF”.

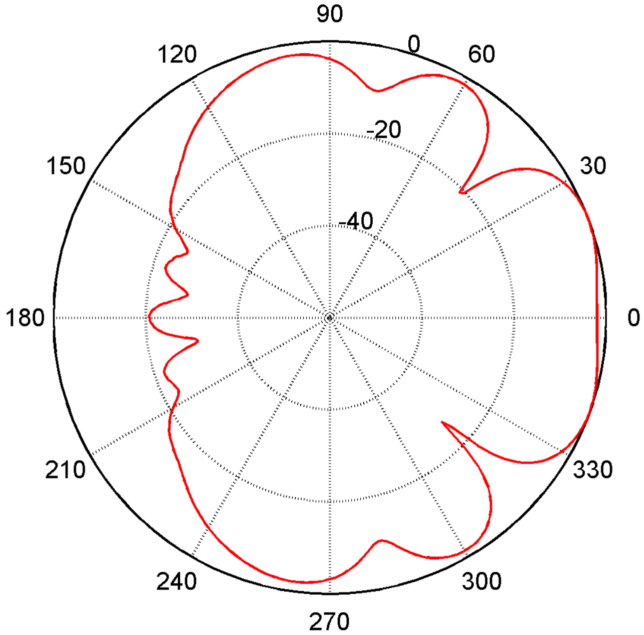

Figure 5.5 Far-field polar directivity plot in dB for the DUREF source at 13.9 kHz.

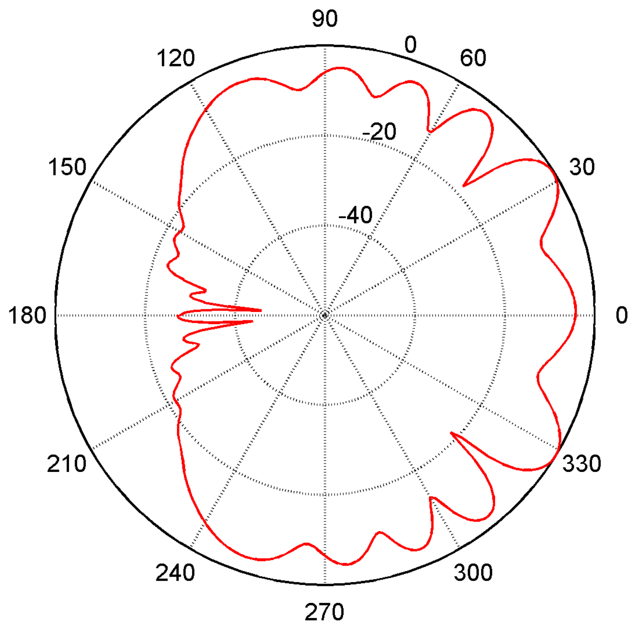

Figure 5.6 Far-field polar directivity plot in dB for the DUREF source at 27.5 kHz.

The DUREF configuration provided the desired directivity features to enable the method to be tested, as is illustrated in Figures 5.5 and 5.6, which show the experimental results of far-field polar directivity plots undertaken a separation distance of 1.22 m. The reflector position corresponds to the 180º direction.

5.3 MEASUREMENTS MADE

Measurements were made of the field produced by the DUAL and DUREF sources for drive frequencies of 13.9 kHz and 27.5 kHz. Both the magnitude and phase of the acoustic pressure field were recorded on cylindrical surfaces surrounding the sources using the facility described in Section 5.1. A B&K8103 hydrophone was used to measure the pressure. This is a small probe hydrophone with a piezoelectric element consisting of an 8 mm long ceramic tube. This gave adequate spatial resolution for the measurements. The hydrophone resonance frequencies at approximately 125 kHz and 270 kHz are well beyond the frequency range of interest for the work undertaken here, leading to an almost constant receiving response of approximately –211 dB re 1V/µPa in the frequency range from 10 kHz to 30 kHz. To generate the cylindrical surfaces, the source transducer was rotated with the hydrophone remaining fixed, as described in Section 5.1, with measurements made at discrete positions on the surface.

The near-field distance for the DUREF source is approximately 0.8 m, calculated using the D^2/λ criterion where D is the maximum dimension of the source and λ is the acoustic wavelength. To ensure measurements are made well into the near-field, the radius of the cylindrical surface must be considerably less than this value.

A cylindrical near-field scan was performed for the DUAL source using a surface of radius 254 mm at both drive frequencies. In addition, at 13.9 kHz only, a scan was also undertaken at a radius of 338 mm. This enabled the prediction method to be exercised and tested using scans on two cylindrical surfaces in the near-field. Measurements were also made on cylindrical surfaces in the acoustic far-field at radial distances of 1.5 m, 2.0 m and 3.0 m.

For the DUREF source, cylindrical near-field scans were performed using a surface of radius 338 mm for both 13.9 kHz and 27.5 kHz. Measurements were also made on cylindrical surfaces in the acoustic far-field at radial distances of 1.2 m, 2.0 m and 3.5 m.

For measurements in the near-field, care must be taken to sample with sufficiently high spatial resolution to avoid aliasing problems. The required sampling interval is typically better than half an acoustic wavelength [29]. To comply with this criterion, the angular increment on the ±180º polar plots (which form the circular data sets) was chosen to be 4.5º for the scans at 13.9 kHz. This corresponds to a sampling rate along the arc of the circle of about 4.0 samples per wavelength for the 338 mm radius scan, and 5.2 points per wavelength for the 254 mm scan. For the 27.5 kHz scans, the angular increment was set to 2.25º, which corresponds to 5.3 points and 4.0 points per wavelength for the scans at 254 mm and 338 mm respectively. The increment for the Z axis translation of the hydrophone (the separation in depth between successive circular data sets) was chosen to be 10 mm, providing 10 and 5 points per wavelength for the scans at 13.9 kHz and 27.5 kHz respectively. The vertical limits of the scan were generally ±475 mm (producing a cylindrical surface of height 950 mm), though some scans were undertaken at ±490 mm.

For the measurements in the far-field, a coarser spacing was acceptable. An angular increment of 4.5º and a vertical increment of 95 mm were used for all far-field scans. To achieve a greater vertical range (a taller cylindrical surface) and thereby capture more of the spreading acoustic field, the far-field scans were undertaken in two stages with the source transducer depth adjusted between stages. The two ±475 mm scans were then combined to provide one larger composite cylindrical scan of 1.9 m in height.

During the measurements, the water temperature was 13.3 ºC and did not vary by more than 0.1 ºC throughout the measurements. The typical time duration for one of the near-field cylindrical scans was about 17 hours, during which time the data acquisition was fully automated under computer control.

A B&K2713 power amplifier was used to drive the source transducer with gains of either 30 dB or 40 dB used, depending on the scan. The drive signals were tone-bursts of the specified frequencies and of duration 0.8 ms to 1.0 ms, generated by an HP3336C waveform generator via a Vinculum E649 gating unit. The drive voltages to the source transducers were of the order of 50 V. A Stanford Research SR560 preamplifier was used to amplify the signal received from the hydrophone, which was then digitised using the HP89410A vector signal analyser.

The raw data files were pre-processed before being passed on to the software described in Section 4. A programme written in the Matlab language was used to read in all the data files for a specific scan and create the arrays of data required by the near-field prediction software.

5.4 MEASUREMENT DATA

The following figures show examples of the near-field data measured on the cylindrical surfaces. In the plots, the amplitude data is shown in decibels referenced to 1 volt. This could be converted to acoustic pressure by scaling the data by the sensitivity of the hydrophone. However, since this is merely a linear scaling, it does not change the amplitude spatial distribution, the conversion has not been performed for the data plotted here. Figures 5.7 shows the amplitude, and Figure 5.8 the phase, for the DUAL source on the cylindrical surface of radius 254 mm. In the plots, the amplitude (or phase) is plotted as a colour-map representing the data values at each point on the cylindrical surface. The data grid has been disabled and interpolation has been used to provide a smooth transition between adjacent data points.

As can be seen, even in the near-field the data shows a high degree of symmetry in the azimuth direction, but greater directivity in the vertical direction, with almost a 20 dB drop in amplitude between the data at the centre of the cylinder and the upper and lower extremities. The phase shows banding on the upper and lower parts of the surface. This is because the phase is plotted as wrapped phase (modulo 2π), with the colour scale going from -180º to +180º. As the hydrophone moves away from the source, the phase cycles through 2π, producing the characteristic bands observed in such plots. Close to the centre of the beam where there is a strong cylindrical wave component, the phase is relatively constant. Again, this is a characteristic of plots of near-field phase data.

Figures 5.9 and 5.10 show amplitude data from two scans on the DUAL source at 13.9 kHz, at radii of 254 mm and 338 mm respectively. With measured data available on two cylinders in the near-field, it is possible to use the boundary element method to predict the outer cylinder distribution using the data from the inner cylinder. The results of performing this analysis are shown later in this report in Section 6.2.

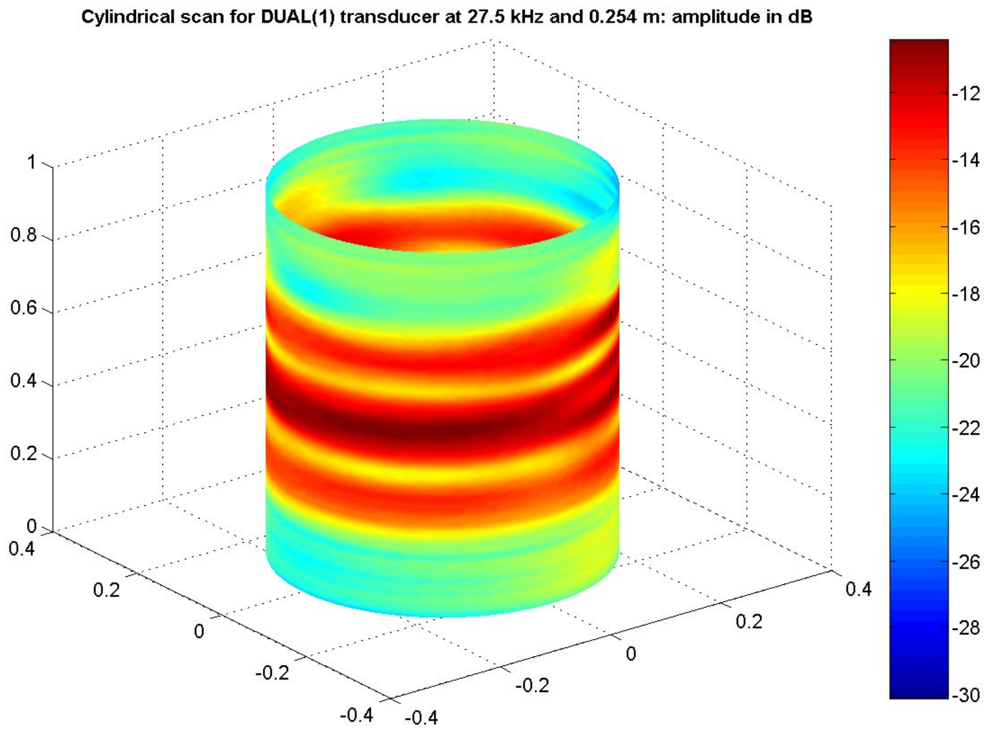

Figure 5.7 Amplitude data from scan on DUAL source at a radius of 254 mm for 27.5 kHz.

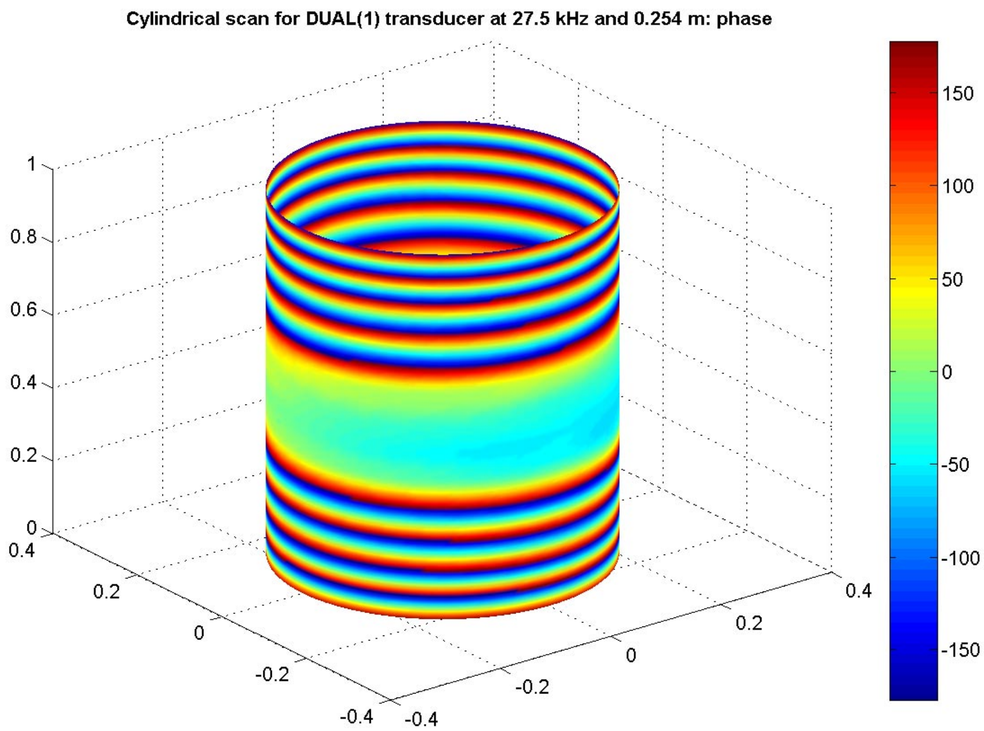

Figure 5.8 Phase data from scan on DUAL source at a radius of 254 mm for 27.5 kHz.

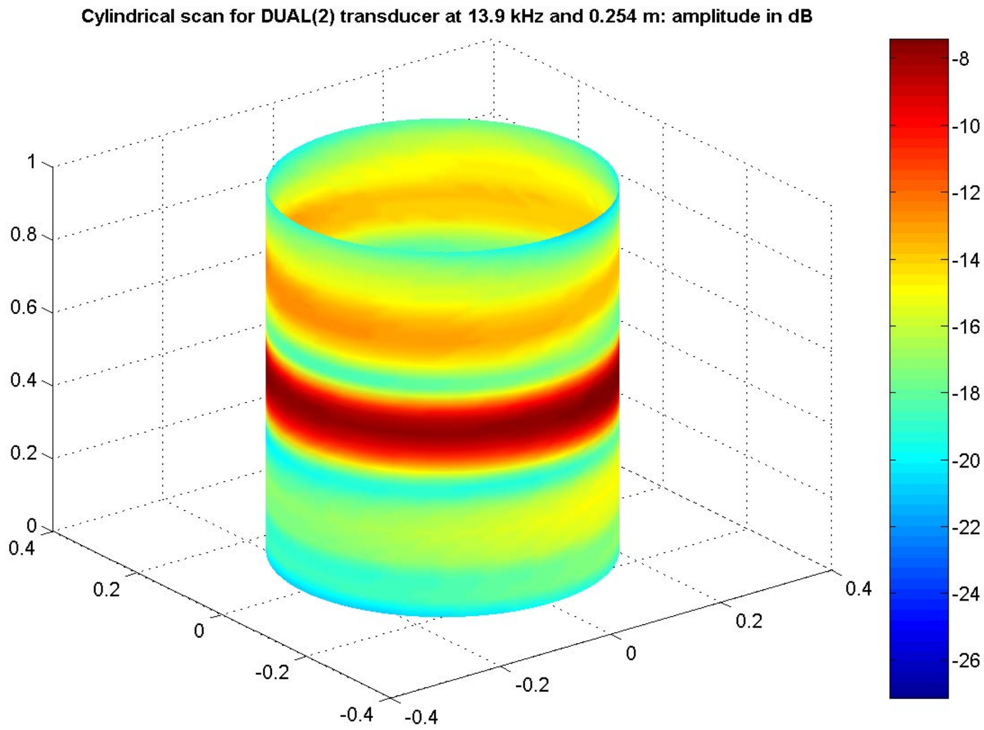

Figure 5.9 Amplitude data from scan on DUAL source at a radius of 254 mm for 13.9 kHz.

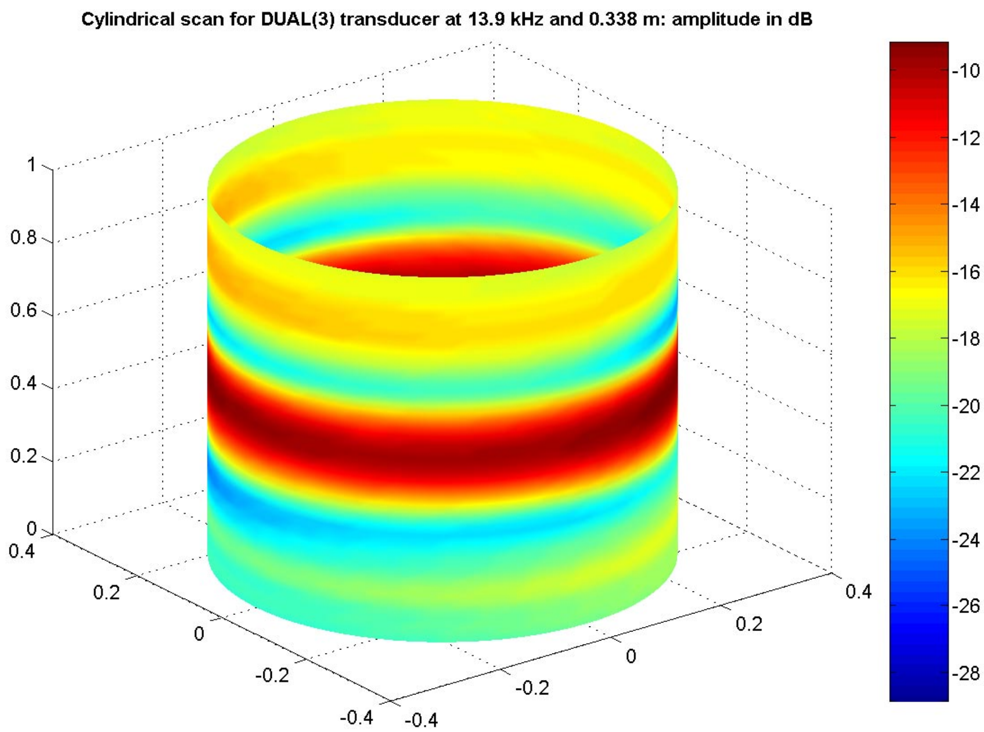

Figure 5.10 Amplitude data from scan on DUAL source at a radius of 338 mm for 13.9 kHz.

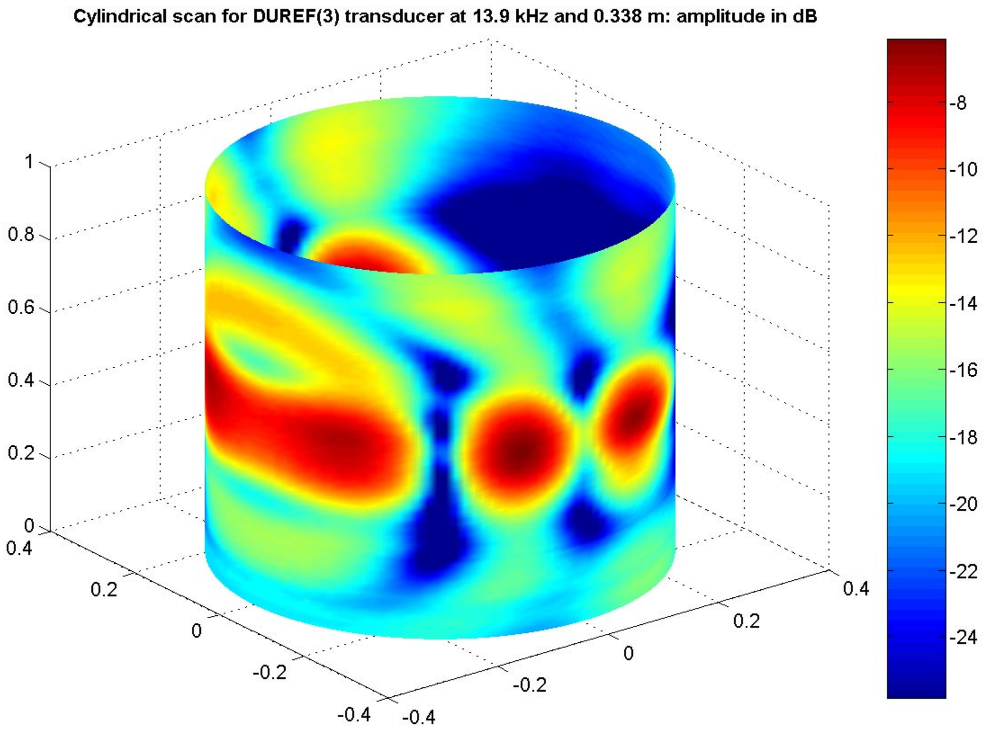

Figure 5.11 Amplitude data for scan on DUREF source at a radius of 338 mm for 13.9 kHz.

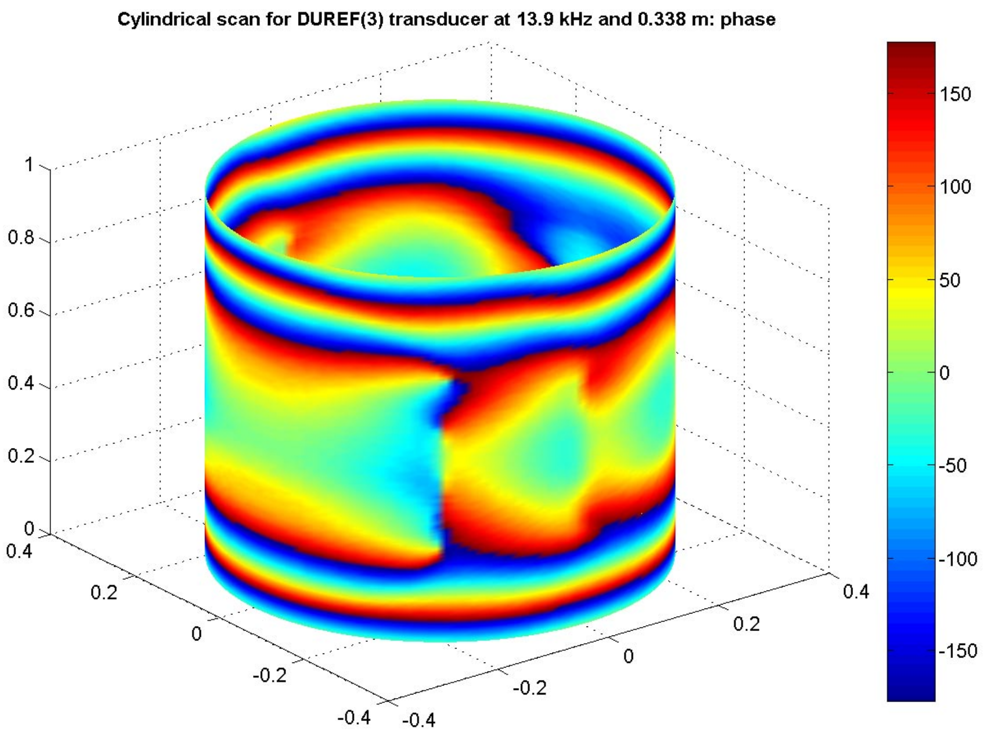

Figure 5.12 Phase data for scan on DUREF source at a radius of 338 mm for 13.9 kHz.

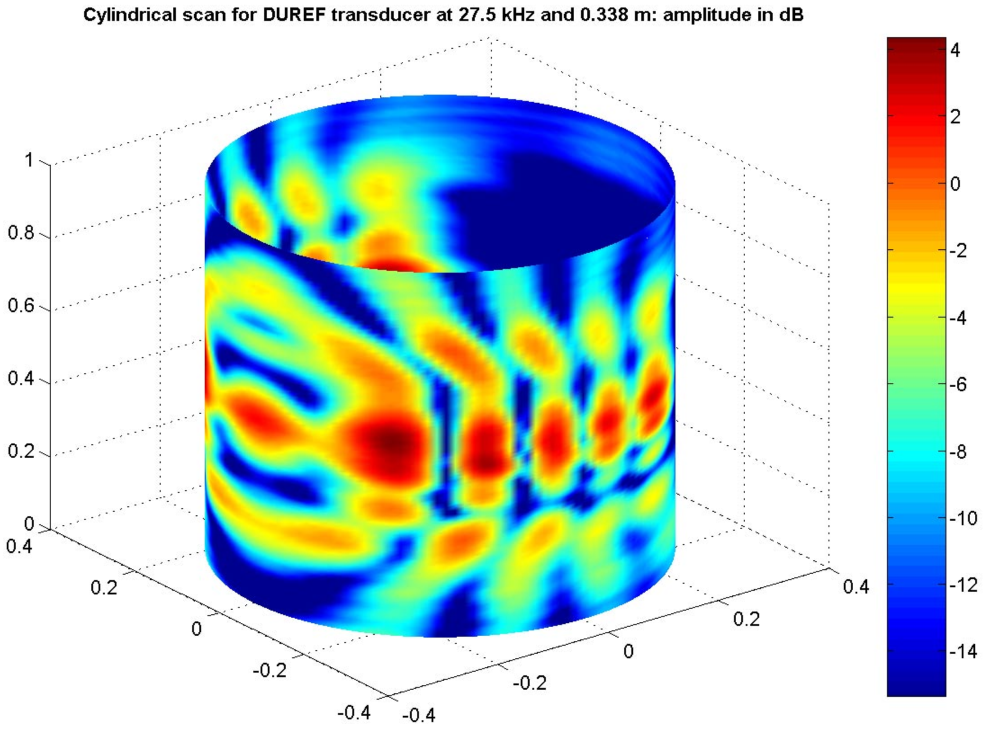

Figure 5.13 Amplitude data for scan on DUREF source at a radius of 338 mm for 27.5 kHz.

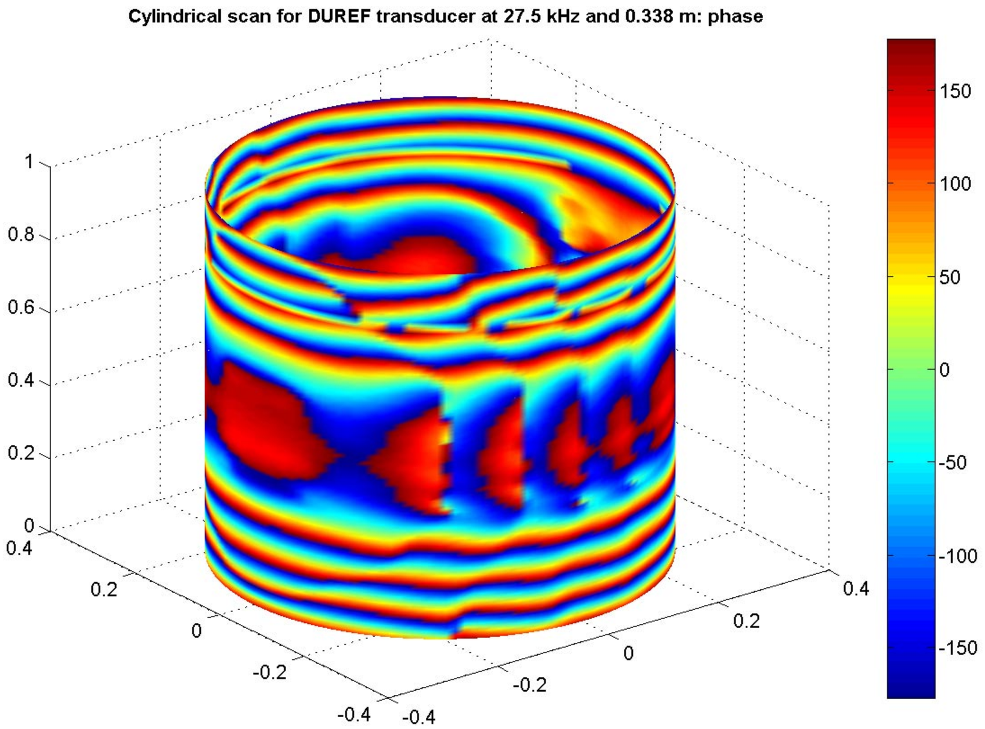

Figure 5.14 Phase data for scan on DUREF source at a radius of 338 mm for 27.5 kHz.

Figure 5.11 and Figure 5.12 show the amplitude and phase distributions respectively for the scan on the DUREF source at a radius of 338 mm for a drive frequency of 13.9 kHz. The interference of the directly radiated signal and that returned from the reflector lead to large variations in the azimuth response, with several lobes clearly visible. Comparison of the two plots shows that positions of nulls in the amplitude distribution correspond to discontinuities in the phase distribution. This is characteristic of such data.

Figure 5.13 and Figure 5.14 show the amplitude and phase distributions respectively for the scan on the DUREF source at a radius of 338 mm for a drive frequency of 27.5 kHz. These plots show the greatest fluctuations in the amplitude and phase distribution, with numerous lobes and nulls visible. The “leakage” of one lobe into another is characteristic of ill-formed beams in the near-field. Once in the far field, these lobes become much more distinct as the acoustic beam becomes fully formed.

6. RESULTS OBTAINED WITH MEASURED NEAR-FIELD DATA

6.1 ACCURACY CONSIDERATIONS

A number of issues have to be considered before the mathematical models and software implementations described in Sections 3 and 4 are applied to the real-world measurements gathered using the techniques described in Section 5. These issues arise from the differences between the idealised theoretical calculations and the real-world practical measurement process, and the need to minimise computational effort. This Section describes the issues and explains the chosen solutions and the rationale behind the choices.

6.1.1 End caps

The main difference between the model and the real measurements is that the model uses a closed surface S, but the measurements are gathered on an open-ended cylinder. This means that the cylinder must be closed using "end caps" before it can be used in the calculations. Additionally, once the shape of the end caps has been chosen, data values must be assigned to each element on the end caps.

Two types of end cap have been considered during this work. The initial development of the software for three-dimensional problems used a hemispherical end cap since this gave opportunities to reduce the number of elements and hence reduce the computational effort. However, if the axisymmetric formulation is used then a hemispherical end cap offers no advantages over a plane circular end cap. Hence, all calculations that have been done using the axisymmetric software have used planar end caps to close off the cylinder.

The question of how to assign pressure values to the end caps has been investigated through a series of tests. Initially it was hoped that assigning zero pressure to all elements on the end caps would suffice, but when this was tried on problems with a known analytical solution, the results were poor. Instead, the pressure was assumed to decrease linearly from the measurement value at the circumference to zero at the centre of the end cap. This method led to satisfactory results, particularly for problems where the amplitude value at the circumference was small compared to the values near the centre of the cylindrical surface.

The requirement that the circumference value at the cylinder ends be small has led to two conflicting aims when choosing the number of measurement lines of constant z that are needed. To minimise computational effort we should use as few lines of data as possible. To maximise accuracy of the results, we should use as many lines as possible. In general, the further away from the transducer the data is measured, the smaller the pressure value is, and so the end cap approximation will have a smaller effect the more data lines are used. It was decided that accuracy was more important than computational effort, particularly since the problem could be distributed across a computational network, and so all of the available data lines were used for each calculation.

6.1.2 Positional accuracy

One of the more problematic aspects of the measurement process is associating an appropriate spatial location with each measurement. It is possible that the calculated results could be highly sensitive to the exact location of the input data, so that good results may depend on good measurement of the radius of the cylinder and the depth at which the measurement is made. Positional errors will affect the amplitude accuracy, but will have an even stronger effect on the phase since any positional error is equivalent to a phase offset of some fraction of an acoustic wavelength. This effect scales with frequency, since the wavelength is shorter at higher frequencies.

The sensitivity to this influence was investigated by running two different calculations using the same set of measurement data. The first calculation assumed that the measurements were made at a radius of 0.3 m, and the second assumed they were made at a radius of 0.338 m.

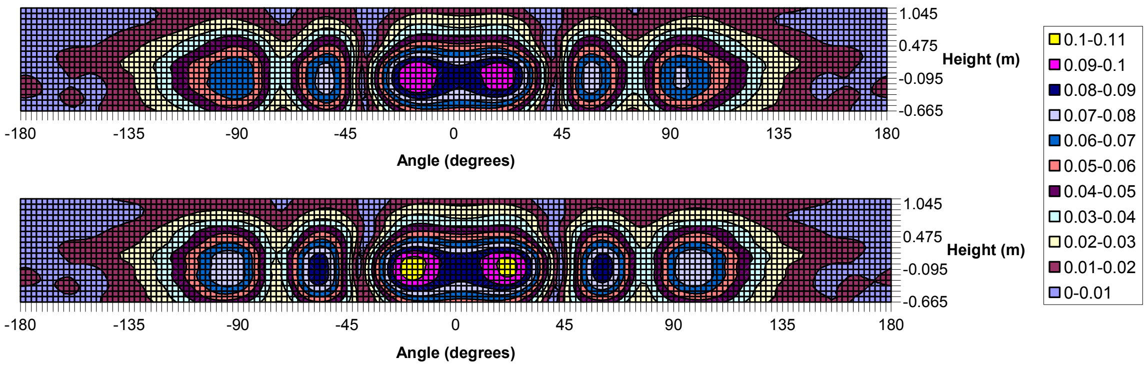

Figure 6.1 Results calculated on a cylinder of radius 2m. The upper plot was calculated from an input surface of radius 0.3 m, and the lower plot was calculated from an input surface of radius 0.338 m.

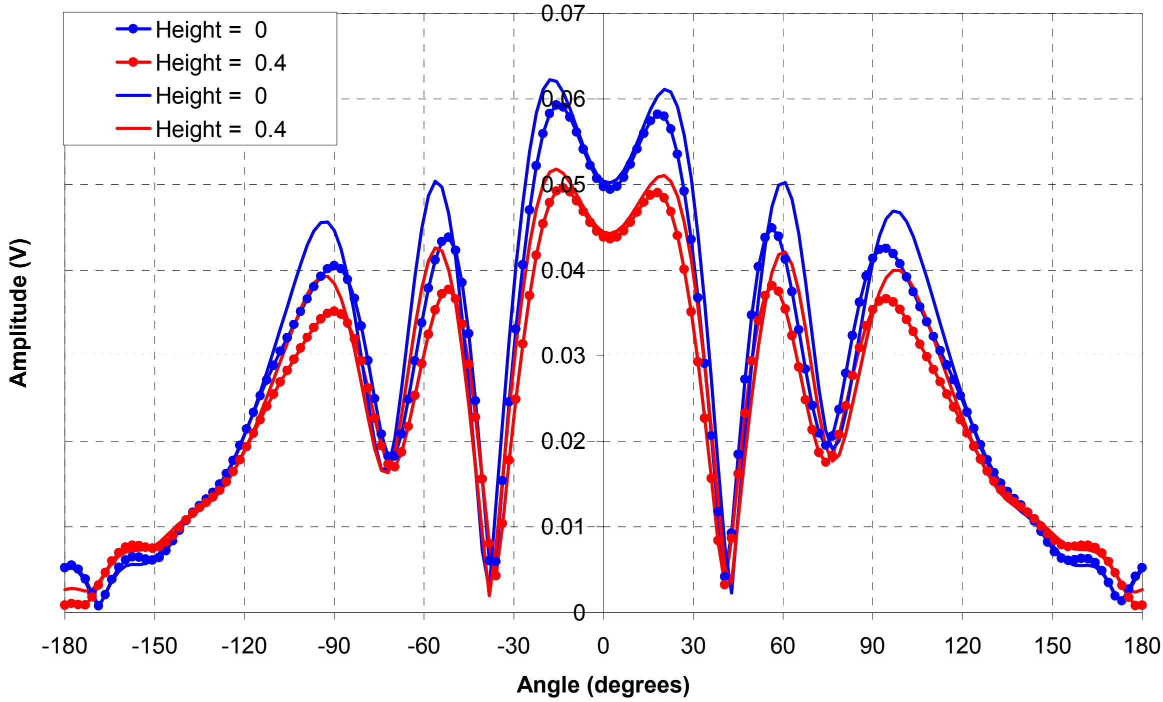

Figure 6.2 Results calculated on a cylinder of radius 3.5 m. The lines with markers were calculated from an input surface of radius 0.3 m, and the lines without markers were calculated from an input surface of radius 0.338 m.

Two typical sets of results are shown in Figures 6.1 and 6.2. All results were calculated on cylinders and the results are plotted as functions of angle and height. Figure 6.1 shows far-field amplitude results calculated at a radius of 2 m, with the upper plot being calculated from an input surface of radius 0.3 m, and the lower one from the input surface of radius 0.338 m. Figure 6.2 shows results calculated at two heights, both at a radius of 3.5 m.

These plots show that the results are sensitive to the accuracy of the location of the points on the input surface, ie the accuracy with which the radius of the surface and the source and hydrophone depth are known. The average difference between the two sets of results is about 10% of the result from the cylinder of 0.338 m radius. The corresponding measurement results matched the 0.338 m cylinder results best. It is interesting to note that, in general, the results from the 0.338 m radius are larger than those from the 0.3 m radius, which is as expected.

6.1.3 Amplifier gain

The method should provide accurate predictions of the absolute values of the far-field response, and not just the spatial distributions. However, to ensure accuracy of the absolute pressures, care must be taken to account for any differences in amplifier gains. As was stated in Section 5.3, the pressures were measured using a B&K8103 hydrophone connected to Stanford Research SR560 preamplifier. A B&K2713 power amplifier was used to drive the source transducers. Both the amplifiers used have variable gains, and the source level on the waveform generator could also be varied. If two sets of measurements have been recorded using different gain settings on any of the amplifiers or on the waveform generator, the pressure measurements will not be to the same scale. In general, the measurements were either recorded using gain settings of –10 dB source, 30 dB power amp, 30 dB pre-amp, -10 dB source, 40 dB power amp, 30 dB pre amp, or -10 dB source, 40 dB power amp, 20 dB pre amp. These settings mean that the scales of the measurements could be made equivalent by multiplying the amplitudes by a factor of √10 where necessary (equivalent to a 10 dB offset in amplification). This factor is only accurate to about 0.25 dB since the values were taken from the front panels of the instruments and not independently measured. This may contribute to the errors in the absolute values calculated in the far-field.

Where the results have been treated in this way, it has not been mentioned explicitly in the text. Wherever absolute numerical results are presented, the values shown are amplitudes measured in volts, without converting the values to acoustic pressure using the hydrophone sensitivity.

6.1.4 Truncation of Fourier series

An issue affecting accuracy of the solution under some circumstances is the choice of the number of Fourier coefficients, N_c, to be used when the infinite sum of Equation (3.18) is truncated for use in a real application. The choice was made to use the smallest value of N_c that satisfies

$$\sqrt{\frac{1}{nm}\sum_{i=1}^{n}\sum_{j=1}^{m}\left[p(\theta_i,z_j)-\hat{p}_j(\theta_i)\right]^2} < 0.05\sqrt{\frac{1}{nm}\sum_{i=1}^{n}\sum_{j=1}^{m}p(\theta_i,z_j)^2}\,, \tag{6.1}$$

where

$$\hat{p}_j(\theta_i) = b_0^j + \sum_{k=1}^{N_c} \left(a_k^j \sin k\theta_i + b_k^j \cos k\theta_i \right), \qquad i = 1,2,\ldots,n,\ j = 1,2,\ldots,m,$$

and $\{p(\theta_i, z_j), i = 1, 2, \ldots, n, j = 1, 2, \ldots, m\}$ are the measured pressures, so that the root mean square (RMS) difference between the Fourier approximations and the measured pressures is less than 5% of the RMS measured pressure. The value of N_c that satisfied this condition generally provided a good approximation to the data and generated good results. Some trials were run with 0.01 (1%) instead of 0.05 (5%) in Equation (6.1), but the difference in the quality of results was not sufficient for the resulting increase in computational effort to be worthwhile.

6.1.5 CHIEF versus Burton-Miller

All the results presented in this Section have been generated using the Fourier formulation of the Burton-Miller method. This choice was made because the Burton-Miller software based on the code of Burton-Miller can run two-dimensional axisymmetric models, whereas the CHIEF software requires a three-dimensional surface. This restriction has two effects: the CHIEF software can only run a job with a comparatively small number of elements on its surface before memory availability becomes a problem; and the CHIEF software cannot be used in conjunction with the Fourier formulation without significant alterations to the source code. The use of the Fourier formulation enables the results to be calculated using the NPL distributed computing network, which means that results can be obtained more quickly and with less disruption to the user than if calculations were run on a single PC. Hence, it was decided that for the results presented here, the software based on the Burton-Miller code of Kirkup would be the best choice.

6.1.6 Variation in water temperature

Any drift in water temperature may also affect the results since the sound speed depends upon the temperature, and any change in the speed of sound will lead to changes in the phase of the acoustic signal. However, the test tank facility has a high degree of temperature stability and the water temperature was stable to within ±0.1 during each of the measurement runs (even on the long runs which could take up to 17 hours). At the temperatures used in the work reported here, a 0.2 ºC change in water temperature leads to about a change in sound speed of about 0.72 m/s (about 0.05%). This is equivalent to only 0.18º of phase, which is not considered to be a significant error.

6.2 COMPARISON OF RESULTS ON NEAR-FIELD SURFACES

The boundary element method can be used for field predictions on more distant surfaces in the near field as well as the far field, because it makes no assumptions that depend for their validity on a large source to receiver distance. To test the quality of the results in the near field, a set of calculations propagating measurement data from a cylinder of radius 0.254 m and height 0.98 m to a concentric cylinder of radius 0.338 m and height 0.98 m was carried out. The results were compared to the actual data measured on the cylinder of radius 0.338 m. The calculation was carried out at a frequency of 13.9 kHz, and the results were calculated on rings every 0.02 m between z = -0.48 m and z = 0.48 m in the vertical direction. All of the measurement data was obtained using the DUAL set-up as described in Section 5.3.

The full set of calculated results and measured data are shown in Figure 6.3. Figure 6.3(a) shows the measured data and 6.3(b) shows the calculated results. The results shown are the amplitude of the measurement; the phase distribution is not shown.

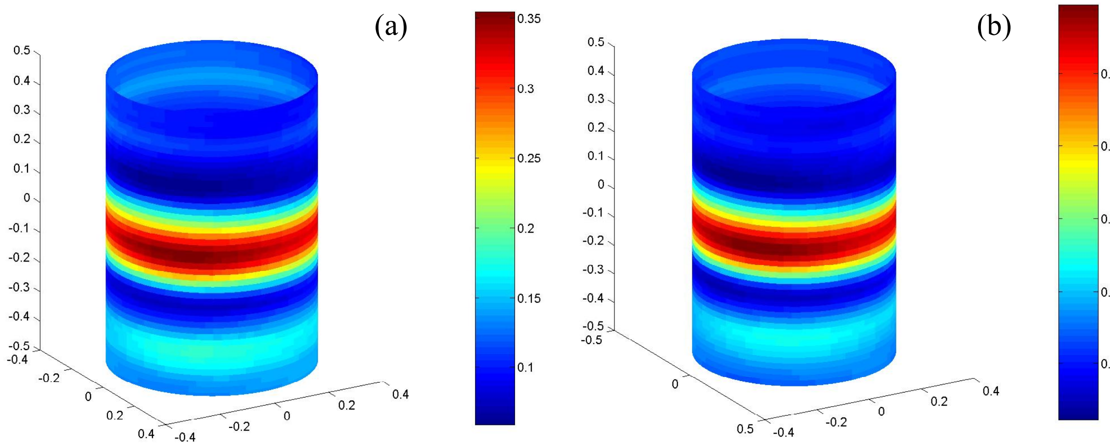

Figure 6.3 Measured data (a) and calculated results (b) on a cylinder of radius 0.338 m, obtained using set-up DUAL at a frequency of 13.9 kHz.

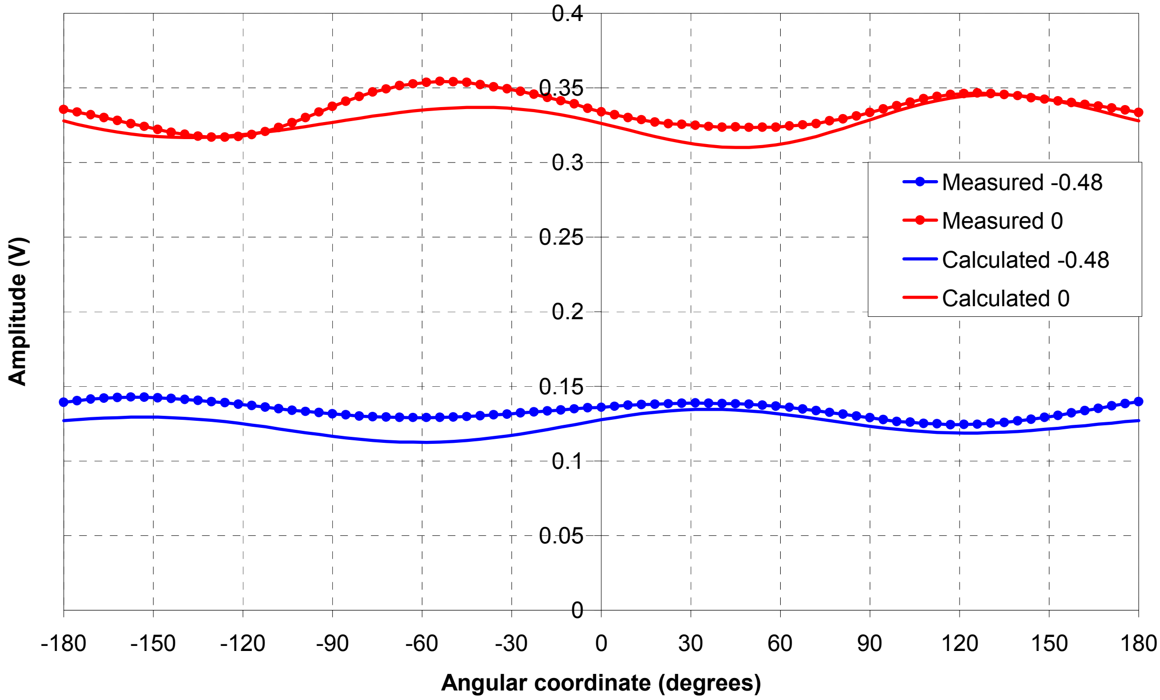

Figure 6.4 Comparison between measured data (lines with symbols) and calculated results (lines with no symbols) for heights z = -0.48 m (blue lines) and z = 0 m (red lines).

Figure 6.4 shows a more detailed quantitative comparison between the rings of calculated results and measured data, one measured at z = -0.48 m, and the other measured at z = 0 m. In both cases, the results show good agreement, both in terms of the absolute amplitude and the variation with angle. The RMS difference between the pairs of lines, relative to the measured result, is about 8% for z = -0.48 m and about 3% for z = 0 m, and in general the measured values are larger than the predicted values.

6.3 COMPARISON WITH MEASURED FAR-FIELD DATA

Figure 6.5 shows a comparison between three different sets of far-field data generated by the DUAL set-up. The results were calculated on a cylinder of radius 3.5 m at heights of 0 m, ± 0.2 m, and ± 0.4 m. The lines with no symbols are measured data. The lines with circles are results calculated by propagating data gathered on a cylinder of radius 0.254 m, and the lines with crosses are results calculated by propagating data gathered on a cylinder of radius 0.338 m. The results shown are all for z = 0 m.

The agreement between the measured data and the results calculated from the cylinder of radius 0.254 m are excellent: the RMS error relative to the measured value is about 1%. The agreement between the results propagated from the cylinder of radius 0.338 m is less impressive but is still good: the RMS error is about 5%. A similar level of agreement is produced for other lines on the cylinder.

Figure 6.6 shows calculated results and measured data from the DUREF set-up at a frequency of 13.9 kHz. The measurement surface is a cylinder of radius 2 m and height 1.805 m. The calculated results were found by propagating measured data from a cylinder of radius 0.338 m and height 0.98 m. Figure 6.6 (a) shows the measured data and Figure 6.6 (b) shows the calculated results. Figure 6.7 shows data (a) and results (b) at a frequency of 27.5 kHz on a cylinder of the same dimensions.

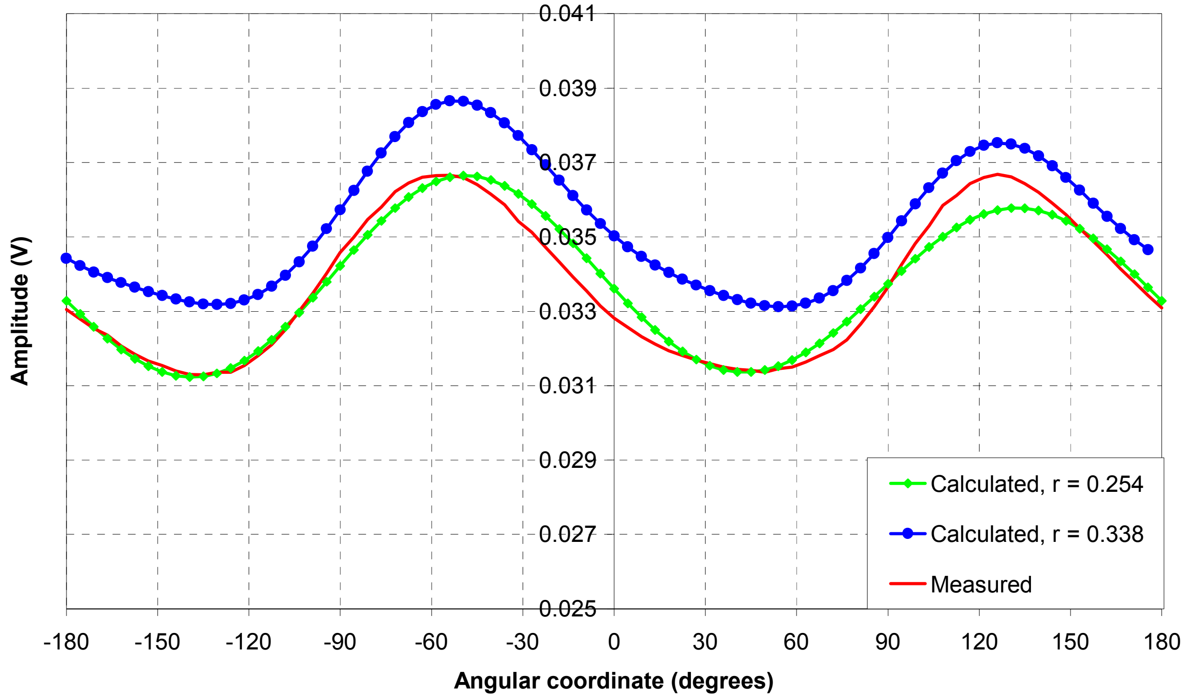

Figure 6.5 Measured far-field data (no symbols) compared with results calculated by propagating data from cylinders of radius 0.254 m (lines with diamonds) and 0.338 m (lines with crosses).

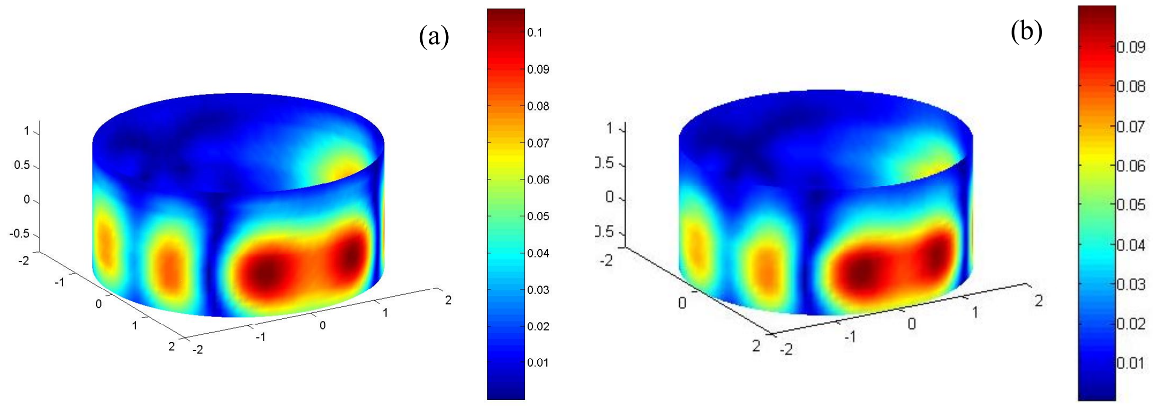

Figure 6.6 Measured data (a) and calculated results (b) on a cylinder of radius 2 m, obtained using source DUREF at a frequency of 13.9 kHz.

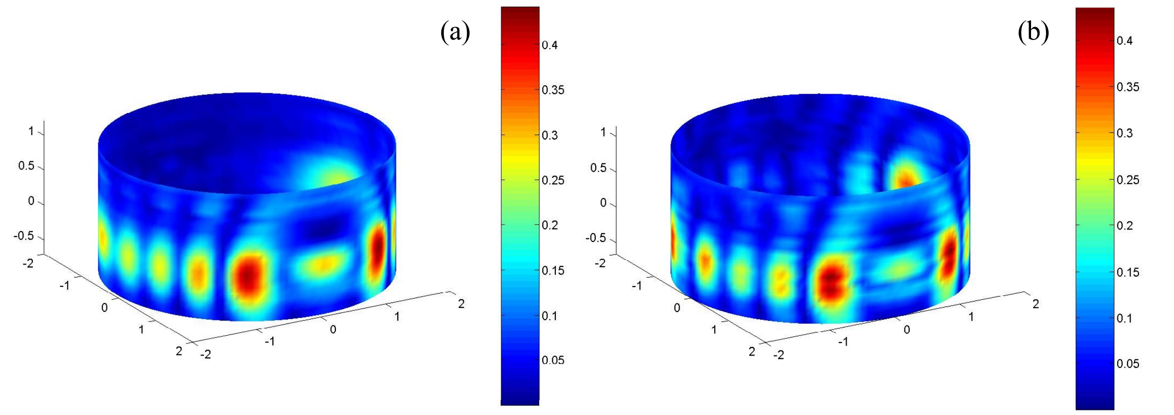

Figure 6.7 Measured data (a) and calculated results (b) on a cylinder of radius 2 m, obtained using source DUREF at a frequency of 27.5 kHz.

In general, the agreement between the calculated results and the measured data is less good at 27.5 kHz than it is at 13.9 kHz. This is illustrated further by the plots in Figures 6.8 and 6.9, which show far-field measurements and predictions for the DUREF source at 13.9 kHz and 27.5 kHz respectively. These measurements and results were obtained at a radius of 3.5 m and $z = 0$ m (results calculated at other values of z exhibit similar behaviour).

As with the results calculated at 2 m, it is clear that the agreement between measurement and calculation is better for a frequency of 13.9 kHz than it is for that of 27.5 kHz. The calculated results for 13.9 kHz in Figure 6.8 show excellent agreement in the position of the main lobes with the side lobes positions agreeing to within around 5º. The peaks of the lobes are generally higher in the measured data by about 8%. In contrast, whilst the 27.5 kHz calculated results seem to show a similar degree of agreement for the main lobes and low order side lobes, they also show extra side lobes at high angles that do not appear in the measured data. Apart from this, the general agreement and overall beam profiles is quite good in both cases.

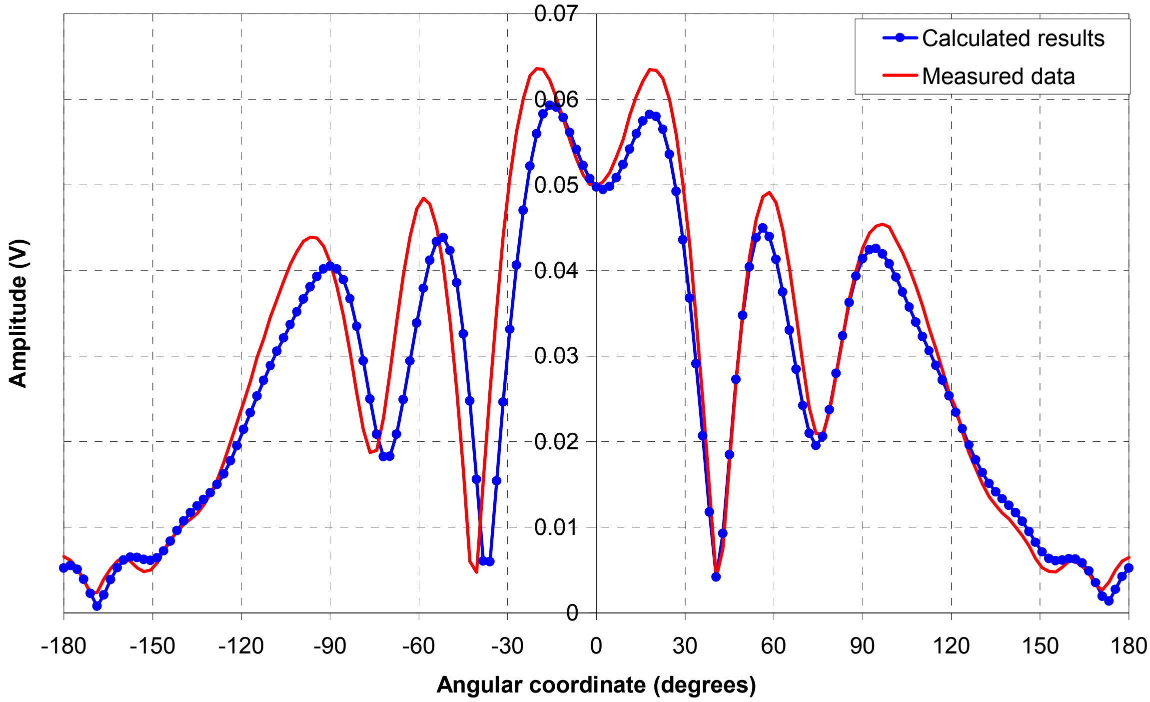

Figure 6.8 Far-field measurement data (red) and calculated results (blue) at 13.9 kHz at a radius of 3.5 m and a height of $z = 0$.

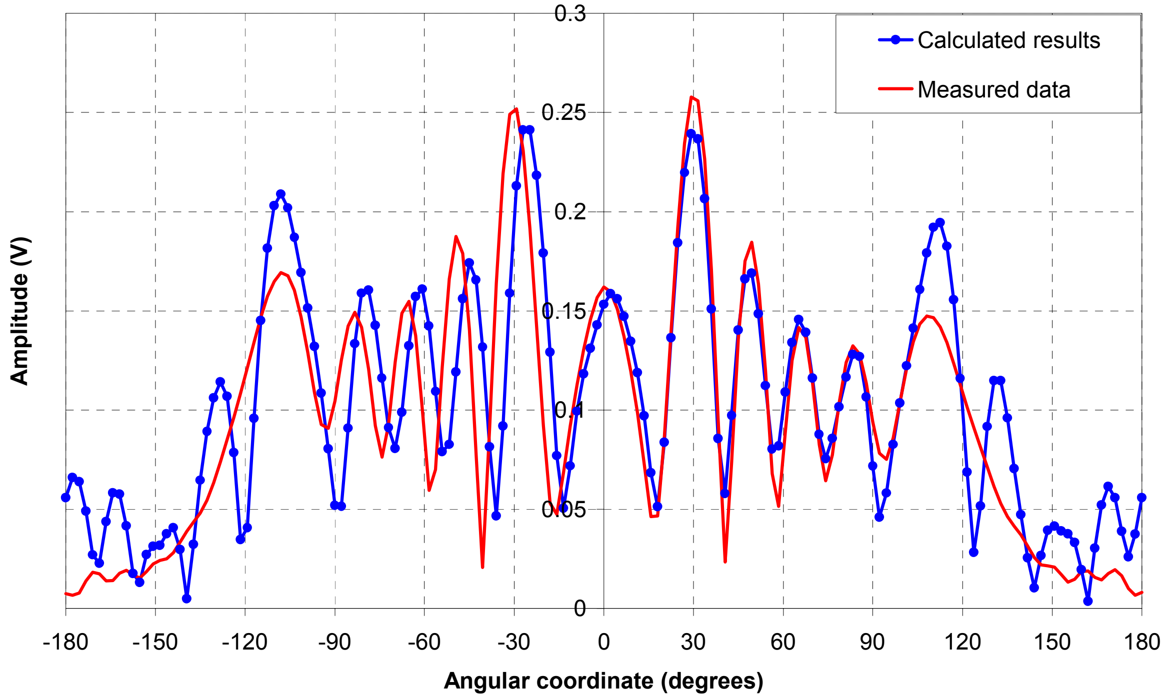

Figure 6.9 Far-field measurement data (red) and calculated results (blue) at 27.5 kHz at a radius of 3.5 m and a height of $z = 0$.

Figures 6.10 and 6.11 show two typical other sets of results, this time obtained from $r = 3.5$ m, $z = -0.4$ m, with the data shown normalised, in decibels, and in the form of polar plots. This type of plot illustrates the spurious side lobes predicted at 27.5 kHz particularly well. These side lobes are predicted to emanate from the "rear" of the source (ie directly through the steel plate) but are not present in the measured far-field data.

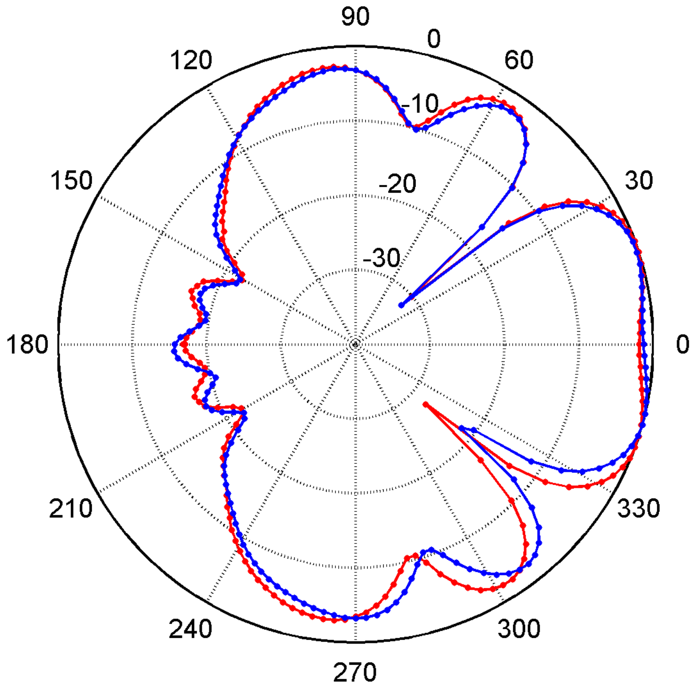

Figure 6.10 Calculated results (blue) and measured data (red) for r = 3.5 m, z = -0.4 m and a frequency of 13.9 kHz. Amplitude in dB.

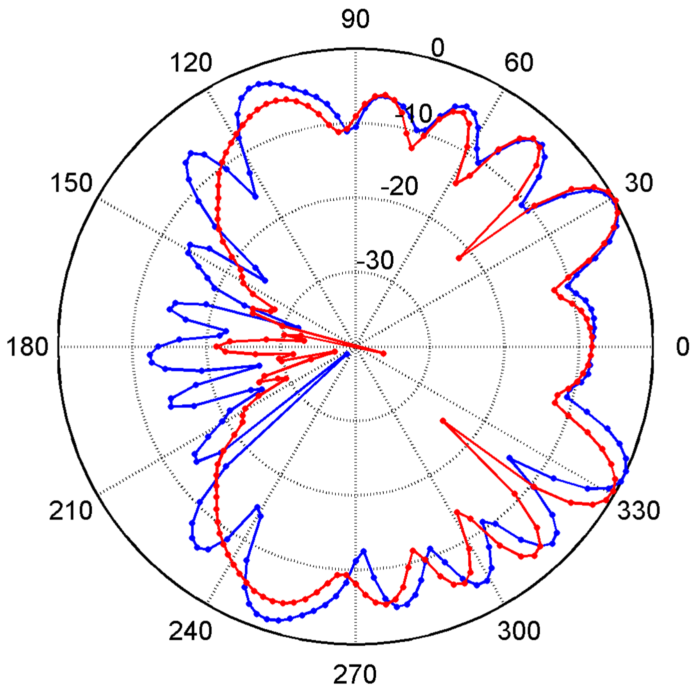

Figure 6.11 Calculated results (blue) and measured data (red) for r = 3.5 m, z = -0.4 m and a frequency of 27.5 kHz. Amplitude in dB.

A definitive cause for the discrepancies has not yet been determined, but there are a number of possible causes. The most likely is that insufficient terms were included in the Fourier series for each circular data set. Such a truncation of a Fourier series can lead to “ringing” in the data in a manner analogous to the so-called Gibbs effect. Since the 27.5 kHz data has a larger number of lobes and therefore contains higher spatial frequencies than the 13.9 kHz data, it is to be expected that the effect would be more significant at the higher frequency. However, militating against this is the fact that the test to decide the required number of terms described in Section 6.1.4 is still passed. Since the test requires that the RMS difference between the Fourier approximated data and the measured pressures on the near-field surface is less than 5% of the RMS measured pressure, this should be sufficient. However, in the region where the deviations are greatest, the magnitude of the pressure is relatively small, and for the regions where the signal level is high, the agreement is good. This may bias the test and mean that it is not sufficient for fields containing high spatial frequencies.

Another possible cause is under sampling of the data, but this is unlikely since care was taken to use a sufficiently fine mesh with at least 4 points per wavelength (see Section 5.3). The truncation of the measured data by having a finite sized cylinder and the need to deal with the issue of populating the end caps may also have an effect. However, it is believed that this would manifest itself by spurious periodicity in the vertical direction (the z direction) rather than in the azimuth orientation. There is some evidence of a variation in agreement between results as the height is varied in the far-field, but this is a relatively minor effect.

Another possible cause is the fact that when the measurements were made there was a fault with the mount for the supporting poles, which led to a slight tilt of the pole away from the vertical. This means that the cylindrical measurement surface tilts inward slightly such that the radius at the top of cylinder is about 20 mm less than that at the bottom (so that the radius varies from 328 mm at the bottom to 348 mm at the top). The effect of this “lampshade” distortion is not yet known.

The cause of these discrepancies, and the sources of error in the method in general, are the subject of ongoing work.

7. CONCLUSIONS

7.1 SUMMARY

A description has been given of work at the National Physical Laboratory to implement near-field techniques to characterise the far-field response of acoustic sources by using boundary-element methods to solve the integral form of the Helmholtz equation. In this manner, it has been possible to predict the far-field response of a source transducer from discrete samples of the complex acoustic pressure measured on cylindrical surfaces in the near-field. A two-stage process was used, first deriving the required pressure gradient on the surface, and then calculating the desired far-field acoustic response. Two methods of overcoming the uniqueness problem inherent in this method have been implemented: the Burton-Miller method, and the CHIEF method. Fourier decomposition of the data from the scans has proven extremely useful in reducing the computational size of the problem.

The state-of-the-art underwater acoustic test facility at NPL (the large Open Tank Facility) was used for the measurements, the precision positioning system enabling automated scans to be performed over the designated surfaces in the near-field of an acoustic source.

Experimental measurements have been made of the field produced by a specially constructed directional source at frequencies of 13.9 kHz and 27.5 kHz. The results of the far-field predictions calculated from the near-field data have been validated by comparison with actual measurements made in the far-field, with agreement achieved of better than 1 dB over much of the acoustic beam-width. The method has been shown to provide valuable data on the far-field response of transducers for cases where the device under test is of high *ka* value such that it may be impossible for far-field conditions to be achieved in a facility of finite size.

The value of using the NPL distributed computing network for this work has been demonstrated. This method is applicable since the use of Fourier decomposition allows the problem to be broken down into smaller sub-units. By computing the individual Fourier coefficients on separate PCs using the distributed network, the computational times have been reduced by a factor of up to 20.

7.2 DISCUSSION

The work undertaken has demonstrated the usefulness of the method for prediction of the acoustic far-field for transducers using data measured in the near-field. However, there are several points worth noting when considering the difficulties of using the method.

The method adopted here is suitable for transducers that exhibit moderate directionality at frequencies of up to mid tens of kilohertz. Transducers which generate high directionality are more difficult to characterise since to satisfy the minimum sampling criterion, a high-density mesh of surface measurements points will be required, increasing the computational size of the problem. Even with Fourier decomposition, a highly collimated beam will contain high spatial frequencies, requiring a large number of terms in the series to be computed. In practical terms, it is also doubtful whether a cylindrical surface is appropriate for such a field since much of the surface will effectively contain very low pressures, or even zero values, with the majority of the sound energy concentrated in a narrow beam. In such cases, a planar geometry is more suitable. At NPL, planar scans coupled with the plane-wave angular spectrum method have been used successfully for directional fields at acoustic frequencies from 100 kHz to 500 kHz.

In the work described here, the method of dealing with the finite height of the cylinder was somewhat empirical. A more rigorous method of closing the end caps would be preferable. In general, it is important to ensure that the field is sampled over a cylinder that is long enough to capture most of the information about the field. If a significant proportion of the field passes through the end caps and is therefore unsampled, this may lead to substantial errors. In practice, this means that the acoustic pressure should have fallen substantially by the top and bottom of the cylinder compared to the value at the centre. In this work, the pressure at the cylinder ends was approximately 20 dB below the maximum value on the surface.

The location of the measurement points on the surface must be fairly accurately known, particularly if absolute values of pressure in the far-field are required. Evidence has been presented in this work that the magnitude of the far-field calculated pressure is sensitive to errors in the measurement of the radius of the cylinder.

Both the Burton-Miller and CHIEF methods were used to overcome the uniqueness problem. Of the two methods, CHIEF is perhaps simpler to implement but has the problem of how to determine the position of the internal co-location points. It is possible to choose a point close to a nodal plane, and this difficulty increases with frequency and the modal density increases. The Burton-Miller method is mathematically more elegant and has the convenience of producing a square system of equations, but has the disadvantage that it is slightly more complex to implement and has a highly singular kernel in the derivative expression (second derivative of the Green's function).

If the Fourier series decomposition of the circular data sets is adopted as in the implementation described here, the problem remains of when to truncate the series without introducing any artefacts into the results.

The cause of the discrepancies noted in this work, and the sources of error in the method in general, are the subject of ongoing work. To continue this work, it is intended that alternative methods for calculating the far-field pressure field will be employed as a comparison and validation of the boundary element methods. For example, the use of an alternative Green's function (as described in Section 2.1) will be attempted. In addition, the use of two-dimensional Fourier techniques based on cylindrical wave-functions will be investigated.

8. ACKNOWLEDGEMENTS

The authors would like to acknowledge the support of the of the National Metrology System Directorate of the UK Department of Trade and Industry which funded this work as part of the 2001-2004 Acoustical Metrology Programme.

9. REFERENCES

1. BOBBER, R. *Underwater electroacoustic measurements.* 1988, Peninsula Press, USA.
2. LURTON, X. *An introduction to underwater acoustics*, 2003, Elsevier.
3. GIANGRECO, C. *Mesures acoustiques appliqués aux antennes sonar*, 1997, Lavoisier, France Commission, Geneva.
4. KINSLER, L. E., FREY, A. E., COPPENS, A. B. and SANDERS, J.V. *Fundamentals of Acoustics*, 1982, Third edition, Wiley and Sons, New York.
5. BAKER, B .B and COPSON, E. T. *The Mathematical Theory of Huygens' Principle,* Oxford at the Clarendon press, 1950.
6. BAKER, D .D. Determination of far-field characteristics of large underwater sound transducers from near-field measurements. *Journal of the Acoustical Society of America*, **34**, p1737-1744, 1962.
7. HORTON, C. W. and INNIS, G. S. The computation of far-field radiation patterns from measurements made near the source. *Journal of the Acoustical Society of America*, **33**, p877-880, 1961.
8. URSELL, F. On the exterior problems of acoustics. *Proceedings of the Cambridge Philosophical Society*, **74**, p117-125, 1973.
9. MARCIANAK, R. D. A nearfield underwater measurement system. *J. Acoust. Soc. Am.* **66**, p955-964, 1979.
10. MEYER, W.L., BELL, W.A., ZINN, B.T. AND STALLYBRASS, M.P. Boundary integral solutions of three dimensional acoustic radiation problems. *Journal of Sound and Vibration* **59**(2), p245–262, 1978.
11. SCHENCK, H.A. Improved integral formulation for acoustic radiation problems. *J. Acoust. Soc. Am.* **44**(1), p41–58, 1968.
12. COPLEY, L.G. Fundamental results concerning integral representations in acoustic radiation. *J. Acoust. Soc. Am.* **44**(1), p28–32, 1968.
13. BURTON, A.J. AND MILLER, G.F. The application of integral equation methods to the numerical solution of some exterior boundary-value problems. *Proc. Roy. Soc. Lond.* A **323**, p201–210, 1971.
14. BURTON, A .J. The solution of Helmholtz's equation in exterior domains using integral equations. *NPL Report NAC 30*, National Physical Laboratory, UK, 1978.
15. FRANCIS, D.T.I. A gradient formulation of the Helmholtz integral equation for acoustic radiation and scattering. *J. Acoust. Soc. Am.* **93**(4), p1700–1709, 1993.
16. E. G. WILLIAMS, *Fourier Acoustics: Sound Radiation and Nearfield Holography*, Academic Press, 1999.
17. P. R. STEPANISHEN AND K. C. BENJAMIN, *Forward and backward projection of acoustic fields using FFT methods*, J. A .S. A., 71 (4), p1158-1164, 1982.
18. R. REIBOLD, *Sound source reconstruction using Fourier optics*, Acustica, 63, p60-64, 1987.

19. M. E. SHAFER AND P. A. LEWIN, *Transducer characterisation using the angular spectrum method*, J. A .S. A., 85 (5), p2202-2214, 1989.

20. PACHNER, J. On the dependence of directivity patterns on the distance from the emitter, *J. Acoust. Soc. Am.* **48**, p86-90, 1956.

21. V.F.HUMPHREY, G.HAYMAN, S.P.ROBINSON AND P.N.GÉLAT Forward and backward propagation of wavefields generated by large aperture transducers. *Proceedings of the Seventh European Conference on Underwater Acoustics, ECUA2004*, p1045–1050, Delft, July 2004. (Pub: TNO, Delft, The Netherlands, ISBN:90-5986-079-9).

22. P. D. THEOBALD, A. D. THOMPSON, S. P. ROBINSON, R. C. PRESTON, P. LEPPER, C. SWIFT, Y. WANG, AND J. TYRER, *Fundamental standards for acoustics based on optical methods – Phase three report for sound in water,* NPL Report CAIR 9, January 2004.

23. VAN BUREN, A. L. Near-field transmitting and receiving properties of planar near-field calibration arrays. *Journal of the Acoustical Society of America*, **89**, p1423-1427, 1991.

24. TROTT, W. J. Underwater sound transducer calibration from nearfield data. *Journal of the Acoustical Society of America*, **53**, p192-199, 1964.

25. VAN BUREN, A. L. Steered planar near-field calibration array. *Journal of the Acoustical Society of America*, **63**, p1052-1059, 1978.

26. VAN BUREN, A. L. Cylindrical near-field calibration array. *Journal of the Acoustical Society of America*, **56**, p849-855, 1974.

27. VAN BUREN, A. L., JEVNAGER, M. D. and TIMS, A. C. A 5 to 50 kHz synthetic cylindrical near-field calibration array. *Journal of the Acoustical Society of America*, **77**, p1927-1932, 1985.

28. VAN BUREN, A. L. Spherical near-field calibration arrays for three-dimensional scanning. *Journal of the Acoustical Society of America*, **85**, p2655-2660, 1989.

29. EARWICKER, M. J. *Sampling errors in near-field measurements on non-planar surfaces*, J. S. V., 66 (2), p255-264, 1979.

30. MACEY, P.C. Oblique Incidence Diffraction by Axisymmetric Structures, *Proc I.O.A.,* **16**(6), p67-74, 1994.

31. KIRKUP, S. The Boundary Element Method in Acoustics, Integrated Sound Software, 1998.

32. COLTON, D. AND KRESS, R. *Inverse Acoustic and Electromagnetic Scattering Theory*, (2nd Edition), Springer, 1998.

33. TERAI, T. On calculation of sound fields around three dimensional objects by integral equation methods. *Journal of Sound and Vibration* **69**(1), p71-100, 1980.

34. GOLUB, G.H. AND VAN LOAN, C.F. *Matrix Computations*. The John Hopkins University Press (third edition), 1996.

35. LAWSON, C.L. AND HANSON, R.J. *Solving Least Squares Problems*. Prentice-Hall, Englewood Cliffs, New Jersey, 1974.

36. ESWARD, T J, JOHNSON, E G, AND WRIGHT, L. Testing Continuous Modelling Software. *NPL Report CMSC 41/04*, March 2004.

37. ESWARD, T J, LEES, K, SAYERS, D, AND WRIGHT, L. Testing Continuous Modelling Software: Three Case Studies. *NPL Report CMSC 42/04*, June 2004.

38. FORSYTHE, S. A Matlab version of CHIEF (Combined Helmholtz Integral Equation Formulation) for solving acoustic radiation and scattering problems, *J. Acoust. Soc. Am.* **106**, p2193, 1999.

39. AMINI, S. On the choice of the coupling parameter in boundary integral formulations of the exterior acoustic problem. *Applicable Analysis*, **35**, p75–92, 1990.

40. AMINI, S. Boundary integral solution for the exterior Helmholtz equation. *Computational Mechanics* **13**, p2–11, 1993.

41. COOK, H, COX, M, DAINTON, M P, AND HARRIS, P M. A Methodology for Testing Spreadsheets and Other Packages Used in Metrology. *NPL Report CISE 25/99*, September 1999.

APPENDIX 1. THE FOURIER SERIES FORMULATION OF THE SURFACE INTEGRAL HELMHOLTZ EQUATION

Consider the form of the Helmholtz equation (3.8) when the bounding surface is axisymmetric. Then in cylindrical polar co-ordinates, if the curve defined by $\zeta(r, z) = 0$ is swept around the z axis to generate the surface, we can write

$$dS_q(r,\theta,z) = d\theta\, d\zeta_q(r,z).$$

Using cylindrical polar coordinates, let $\mathbf{p} = (r_p, \theta_p, z_p)$ and $\mathbf{q} = (r_q, \theta_q, z_q)$. Define a function ε such that

$$\varepsilon(r,\theta,z) = \begin{cases} \frac{1}{2}, & (r,\theta,z) \in S, \\ 1, & (r,\theta,z) \in E, \end{cases}$$

for ease of notation, and Equation (3.8) becomes

$$\begin{aligned} \varepsilon(r_p,\theta_p,z_p)\varphi(r_p,\theta_p,z_p) = & \int_{-\pi}^{\pi}\int_{\zeta} \varphi(r_q,\theta_q,z_q)\frac{\partial}{\partial n_q} G_k(r_p,\theta_p,z_p,r_q,\theta,z_q) d\zeta_q(r_q,z_q) d\theta_q \\ & - \int_{-\pi}^{\pi}\int_{\zeta} G_k(r_p,\theta_p,z_p,r_q,\theta_q,z_q)\frac{\partial}{\partial n_q}\varphi(r_q,\theta_q,z_q) d\zeta_q(r',z') d\theta_q \end{aligned} \tag{A1}$$

In cylindrical polar coordinates, the Green's function is

$$G_k(r,\theta,z,r',\theta',z') = \frac{e^{ikR}}{4\pi R},$$

where

$$\begin{aligned} R^2 &= (r\cos\theta - r'\cos\theta')^2 + (r\sin\theta - r'\sin\theta')^2 + (z - z')^2 \\ &= r^2 + r'^2 - 2rr'\cos(\theta - \theta') + (z - z')^2, \end{aligned}$$

and so for **p** and **q** as stated above, G_k is a function of $\cos(\theta_p - \theta_q)$. Hence G_k is periodic with period 2π. Additionally,

$$G_k(r,\theta,z,r',\theta',z') = G_k(r,0,z,r',\theta' - \theta,z')$$

Consider a more general form of (3.18) where the pressure p is a continuous function of r and z. The coefficients a_k^j and b_k^j are replaced by continuous functions of r and z, $a_k(r, z)$ and $b_k(r, z)$, so that (3.18) becomes

$$p(r,\theta,z) = b_0 + \sum_{k=1}^{\infty}\{a_k(r,z)\sin k\theta + b_k(r,z)\cos k\theta\}. \tag{A2}$$

Substituting this Fourier series into the left hand side of (A1), multiplying by $\cos(m\theta_p)$, and integrating with respect to θ_p between $-\pi$ and π, gives

$$\pi\varepsilon(r_p,\theta_p,z_p)b_m(r_p,z_p).$$

Doing the same to the right hand side of (A1) gives

$$\begin{aligned}&\int_{-\pi}^{\pi}\int_{-\pi}^{\pi}\int_{\zeta}\left\{b_0+\sum_{n=1}^{\infty}\left[a_n\sin(n\theta_q)+b_n\cos(n\theta_q)\right]\right\}\frac{\partial}{\partial n_q}G_k d\zeta_q d\theta_q\cos(m\theta_p)d\theta_p\\&-\int_{-\pi}^{\pi}\int_{-\pi}^{\pi}\int_{\zeta}G_k\frac{\partial}{\partial n_q}\left\{b_0+\sum_{n=1}^{\infty}\left[a_n\sin(n\theta_q)+b_n\cos(n\theta_q)\right]\right\}d\zeta_q d\theta_q\cos(m\theta_p)d\theta_p,\end{aligned} \tag{A3}$$

where the a_n and b_n are functions of r_q and z_q, and where $d\zeta_q = d\zeta_q(r_q, z_q)$ and $G_k = G_k(r_p, \theta_p, z_p, r_q, \theta_q, z_q)$. Consider the first term in this expression. The direction normal to an axisymmetric surface is always perpendicular to the θ direction in cylindrical polar coordinates, so the normal derivative of a function of θ is zero. Hence

$$\frac{\partial}{\partial n_q}G_k(r,\theta_p,z,r_q,\theta_q,z_q)$$

will be a function of $\cos(\theta_p - \theta_q)$. By the same argument, in the second term

$$\frac{\partial}{\partial n_q}\left\{b_0+\sum_{n=1}^{\infty}\left[a_n\sin(n\theta_q)+b_n\cos(n\theta_q)\right]\right\}=\frac{\partial b_0}{\partial n_q}+\sum_{n=1}^{\infty}\left[\frac{\partial a_n}{\partial n_q}\sin(n\theta_q)+\frac{\partial b_n}{\partial n_q}\cos(n\theta_q)\right].$$

From the form of G_k given above, the first term in (A3) is

$$\int_{-\pi}^{\pi}\int_{-\pi}^{\pi}\int_{\zeta}\left\{b_0+\sum_{n=1}^{\infty}\left[a_n\sin(n\theta_q)+b_n\cos(n\theta_q)\right]\right\}\cos(m\theta_p)\frac{\partial}{\partial n_q}G_k(r_p,0,z_p,r_q,\theta_q-\theta_p,z_q)d\zeta_q d\theta_q d\theta_p.$$

Changing the order of integration and writing $\theta_p = \theta_q - \alpha$ in this expression gives

$$\int_{\zeta}\int_{-\pi}^{\pi}\int_{\theta_q-\pi}^{\theta_q+\pi}\left\{b_0+\sum_{n=1}^{\infty}\left[a_n\sin(n\theta_q)+b_n\cos(n\theta_q)\right]\right\}\cos(m[\theta_q-\alpha])\frac{\partial}{\partial n_q}G_k d\alpha d\theta_q d\zeta_q.$$

Expanding using

$$\cos(m[\theta_q-\alpha])=\cos(m\theta_q)\cos(m\alpha)+\sin(m\theta_q)\sin(m\alpha)$$

and rearranging terms gives

$$\int_{\zeta}\int_{-\pi}^{\pi}\left\{b_0+\sum_{n=1}^{\infty}\left[a_n\sin(n\theta_q)+b_n\cos(n\theta_q)\right]\right\}\cos(m\theta_q)\left[\int_{\theta_q-\pi}^{\theta_q+\pi}\cos(m\alpha)\frac{\partial}{\partial n_q}G_k(r_p,0,z_p,r_q,\alpha,z_q)d\alpha\right]d\theta_q d\zeta_q$$

$$+\int_{\zeta}\int_{-\pi}^{\pi}\left\{b_0+\sum_{n=1}^{\infty}\left[a_n\sin(n\theta_q)+b_n\cos(n\theta_q)\right]\right\}\sin(m\theta_q)\left[\int_{\theta_q-\pi}^{\theta_q+\pi}\sin(m\alpha)\frac{\partial}{\partial n_q}G_k(r_p,0,z_p,r_q,\alpha,z_q)d\alpha\right]d\theta_q d\zeta_q.$$

It was shown above that G_k and its normal derivative are periodic with period 2π. Since m and n are integers, $\cos(m\alpha) = \cos(m[\alpha + 2\pi])$ and $\sin(m\alpha) = \sin(m[\alpha + 2\pi])$.

These properties mean that the two functions being integrated with respect to α are periodic functions that are integrated over one full period. This means that the integration is independent of the θ_q that appears in the limits of integration. Without loss of generality, the integration limits can be set to $-\pi$ and π. Since G_k is an even function of α and $\sin(m\alpha)$ is an odd function of α, the integral of their product between $-\pi$ and π must be zero, and so the second bracketed term vanishes.

It can be shown that

$$\int_{-\pi}^{\pi}\cos(m\theta)\cos(m\theta)d\theta=\int_{-\pi}^{\pi}\sin(m\theta)\sin(m\theta)d\theta=\pi\delta_{mn},$$

and

$$\int_{-\pi}^{\pi}\cos(m\theta)\sin(m\theta)d\theta=0,$$

which means that all the terms in the summation vanish apart from that featuring b_m. Hence the only remaining terms in the expression are

$$\pi\int_{\zeta}b_m(r_q,z_q)\int_{-\pi}^{\pi}\cos(m\alpha)\frac{\partial}{\partial n_q}G_k(r_p,0,z_p,r_q,\alpha,z_q)d\alpha d\zeta_q(r_q,z_q).$$

By the same arguments, the second term in (3.19) becomes

$$\pi\int_{\zeta}\frac{\partial b_m}{\partial n_q}(r_q,z_q)\int_{-\pi}^{\pi}\cos(m\alpha)G_k(r_p,0,z_p,r_q,\alpha,z_q)d\alpha d\zeta_q(r_q,z_q),$$

and so the Helmholtz equation becomes

$$\int_{\zeta} b_m(r_q, z_q) \int_{-\pi}^{\pi} \cos(m\alpha) \frac{\partial}{\partial n_q} G_k(r_p, 0, z_p, r_q, \alpha, z_q) d\alpha d\zeta_q(r_q, z_q)$$
$$- \int_{\zeta} \frac{\partial b_m}{\partial n_q}(r_q, z_q) \int_{-\pi}^{\pi} \cos(m\alpha) G_k(r_p, 0, z_p, r_q, \alpha, z_q) d\alpha d\zeta_q(r_q, z_q) = \varepsilon(r_p, z_p) b_m(r_p, z_p). \tag{A4}$$

A similar set of arguments apply if both sides are multiplied by sin($m\theta$) and integrating. The resulting expression becomes

$$\int_{\zeta} a_m(r_q, z_q) \int_{-\pi}^{\pi} \cos(m\alpha) \frac{\partial}{\partial n_q} G_k(r_p, 0, z_p, r_q, \alpha, z_q) d\alpha d\zeta_q(r_q, z_q)$$
$$- \int_{\zeta} \frac{\partial a_m}{\partial n_q}(r_q, z_q) \int_{-\pi}^{\pi} \cos(m\alpha) G_k(r_p, 0, z_p, r_q, \alpha, z_q) d\alpha d\zeta_q(r_q, z_q) = \varepsilon(r_p, z_p) a_m(r_p, z_p). \tag{A5}$$

Expressions (A4) and (A5) mean that if a function $G_k^m(r_p, z_p, r_q, z_q)$ is defined as

$$G_k^m(r_p, z_p, r_q, z_q) = \int_{-\pi}^{\pi} \cos(m\alpha) G_k(r_p, 0, z_p, r_q, \alpha, z_q) d\alpha,$$

then the coefficients a_m and b_m obey

$$\int_{\zeta} c_m(\mathbf{q}) \frac{\partial}{\partial n_q} G_k^m(\mathbf{p}, \mathbf{q}) - G_k^m(\mathbf{p}, \mathbf{q}) \frac{\partial}{\partial n_q} c_m(\mathbf{q}) d\zeta_q = \begin{cases} \frac{1}{2} c_m(\mathbf{p}), & \mathbf{p} \in S, \\ c_m(\mathbf{p}), & \mathbf{p} \in E, \end{cases} \tag{A6}$$

where c_m is one of the a_m and b_m. This is effectively a two-dimensional form of Equation (3.8).

Note that Equation (A5) still features a cosine term in the integration with respect to α even though the a_m relate to sine terms in the Fourier expansion. This is caused by using the expansion

$$\sin(m[\theta_q - \alpha]) = \sin(m\theta_q)\cos(m\alpha) - \cos(m\theta_q)\sin(m\alpha).$$

If a sine term is used instead, which in some respect may seem more natural for a sine Fourier coefficient, the results will of course be incorrect.